THE JOURNAL OF BIOLOGICAL CHEMISTRY VOL. 290, NO. 16, pp. 10274–10294 , April 17, 2015

Processivity of the Kinesin-2 KIF3A Results from Rear Head Gating and Not Front Head Gating*[S]

Received for publication, November 24, 2014, and in revised form, January 30, 2015 Published, JBC Papers in Press, February 5, 2015, DOI 10.1074/jbc.M114.628032

Geng-Yuan Chen, David F. J. Arginteanu, and William O. Hancock[1]
From the Department of Biomedical Engineering Pennsylvania State University University Park, Pennsylvania 16802

Background: KIF3A/B is less processive than kinesin-1, particularly under load.
Results: In an engineered KIF3A dimer, intramolecular strain in the two-head-bound state does not alter nucleotide binding. In ADP, the motor dissociates slowly from microtubules.
Conclusion: KIF3A lacks front head gating and maintains processivity through weak microtubule binding.
Significance: During bidirectional transport, kinesin-2 is expected to detach more readily than kinesin-1.

The kinesin-2 family motor KIF3A/B works together with dynein to bidirectionally transport intraflagellar particles, melanosomes, and neuronal vesicles. Compared with kinesin-1, kinesin-2 is less processive, and its processivity is more sensitive to load, suggesting that processivity may be controlled by different gating mechanisms. We used stopped-flow and steady-state kinetics experiments, along with single-molecule and multimotor assays to characterize the entire kinetic cycle of a KIF3A homodimer that exhibits motility similar to that of full-length KIF3A/B. Upon first encounter with a microtubule, the motor rapidly exchanges both mADP and mATP. When adenosine 5′-[(β,γ)-imido]triphosphate was used to entrap the motor in a two-head-bound state, exchange kinetics were unchanged, indicating that rearward strain in the two-head-bound state does not alter nucleotide binding to the front head. A similar lack of front head gating was found when intramolecular strain was enhanced by shortening the neck linker domain from 17 to 14 residues. In single-molecule assays in ADP, the motor dissociates at 2.1 s^{-1}, 20-fold slower than the stepping rate, demonstrating the presence of rear head gating. In microtubule pelleting assays, the K_D^{Mt} is similar in ADP and ATP. The data and accompanying simulations suggest that, rather than KIF3A processivity resulting from strain-dependent regulation of nucleotide binding (front head gating), the motor spends a significant fraction of its hydrolysis cycle in a low affinity state but dissociates only slowly from this state. This work provides a mechanism to explain differences in the load-dependent properties of kinesin-1 and kinesin-2.

The kinesin-2 motor KIF3A/B transports intraflagellar particles in cilia and flagella, pigment granules in melanosomes, and vesicles in neurons (1–4). Deficiencies in these transport processes are implicated in polycystic kidney disease and neurodegenerative diseases (4–6). Kinesin-2 motors work together with dynein to transport cargo bidirectionally along microtubules, and the mechanisms underlying the regulation of this bidirectional transport are hotly debated (7). In some cases, kinesin-1 and kinesin-2 are found on the same cargo for reasons that are not entirely clear (8, 9). Part of this lack of clarity has arisen because, although kinesin-1 has been the subject of extensive study, little is known regarding differences between the kinesin-1 and kinesin-2 chemomechanical cycles.

Due to similarities in sequence and motor characteristics, the stepping mechanism of kinesin-2 is thought to be qualitatively the same as kinesin-1. Kinesin-1 steps in a hand-over-hand manner (10–13) at a rate of 100 steps/s (14) and can walk against hindering loads approaching 6 piconewtons (15, 16). Kinesin-1 is highly processive, taking 100 or more steps before detaching (17), which results from tight coordination between the hydrolysis cycles of the two heads. Compared with kinesin-1, kinesin-2 shows a similar stall force, a velocity roughly half of kinesin-1, and run lengths of roughly one-fourth of kinesin-1 (18, 19), implying less head-head coordination.

The gating mechanisms underlying kinesin-1 processivity have been the subject of intense investigation, but they are not entirely resolved, and the degree to which these gating mechanisms extend to other kinesins is also not clear. The key to kinesin processivity is maintaining the hydrolysis cycles of the two heads out of phase, such that at least one head is bound to the microtubule at all times. The two prominent (nonexclusive) mechanisms to achieve this are front head gating and rear head gating (20–25). Front head gating holds that when both heads are bound to the microtubule, rearward tension on the front head inhibits ATP binding, such that the rear head detaches before ATP binding and stepping by the front head can occur (22, 24, 25). In contrast, the rear head gating model holds that binding of the front head accelerates detachment of the trailing head from the microtubule, implying that processivity results primarily from the fact that dissociation from the one-head-bound state is slower than the overall hydrolysis cycle (20, 21).

The most direct evidence for front head gating in kinesin-1 is the finding that when the motor is locked in the two-head-bound state by AMPPNP,[2] the on-rate for binding of mADP is 80-fold slower than in the unstrained one-head-bound state

* This work was supported, in whole or in part, by National Institutes of Health Grant R01 GM076476 (to W. O. H.).
[S] This article contains supplemental code.
[1] To whom correspondence should be addressed: Dept. of Biomedical Engineering, Penn State University, 205 Hallowell Bldg., University Park, PA 16802. Tel.: 814-863-0492; Fax: 814-863-0492; E-mail: wohbio@engr.psu.edu.

[2] The abbreviations used are: AMPPNP, adenosine 5′-[(β,γ)-imido]triphosphate; ACES, 2-[(2-amino-2-oxoethyl)amino]ethanesulfonic acid; mant-, 2′-(or-3′)-*O*-(*N*-methylanthraniloyl) group; mATP, mant-ATP; mADP, mant-ADP; mAMPPNP, mant-AMPPNP; Mt, microtubule; ATPγS, adenosine 5′-*O*-(thiotriphosphate); FH, front head; HS, half-site experiment; TIRF, total internal reflection fluorescence.

(24). Further support comes from the finding that release from such a two-head-bound state requires a back-step before forward stepping resumes (22). Strain-dependent nucleotide binding and phosphate release experiments also support the front head gating model in kinesin-1 (22, 23, 26). Structurally, the inhibition of nucleotide binding could result from a mechanical deformation of the front head, or it could be a consequence of the specific conformation of the motor domain that results when the neck linker is physically prevented from docking.

We found previously that processivity differences between kinesin-1 and kinesin-2 could be entirely accounted for by differences in their neck linker lengths and that for motors in other kinesin families, shortening the neck linker to the 14-residue length in kinesin-1 also increases their processivity (18, 27). This dependence on neck linker length was attributed to the change in interhead tension that results from extending the elastic element connecting the two motor domains. From stochastic simulations, neither front head gating nor rear head gating alone was sufficient to explain the processivity and velocity dependence on neck linker length, but results could be quantitatively accounted for by a model in which interhead tension modulates both front and rear head gating (18).

The goal of the present work was to uncover the kinetic mechanisms underlying kinesin-2 processivity by investigating the biochemical kinetics of a homodimeric KIF3A motor that was shown previously to have velocity, run length, and load-dependent properties similar to those of full-length KIF3A/B (18, 28, 29). To test for the presence of rear head gating, the dissociation rate of KIF3A from microtubules in the low affinity ADP state was measured and compared with the normal motor stepping rate. In ADP, KIF3A dimer dissociates from microtubules at a rate 20-fold slower than the motor stepping rate in saturating ATP, meaning that during stepping, detachment of the rear head is accelerated ("gated") by the activity of the leading head. To test for front head gating, the motor was locked in a two-head-bound state, and the rate of nucleotide binding to the strained front head was measured. Front head nucleotide exchange was identical to unstrained rates, meaning that nucleotide binding ("gating") of the front head is not altered by the activity of the trailing head. Thus, the processivity of KIF3A results from a rear head gating mechanism in which the motor dissociates slowly from the microtubule, and fast stepping is achieved by strain-dependent detachment of the trailing head.

EXPERIMENTAL PROCEDURES

Protein Constructs, Purification, and Quantification—All KIF3A constructs consist of the head and neck linker domain of *Mus musculus* KIF3A, fused to the coiled-coil of *Drosophila* KHC. Details of the GFP-labeled constructs as well as their bacterial expression and nickel column purification were described previously (18). $KIF3A_{17}$ and $KIF3A_{14}$ refer to equivalent constructs truncated at amino acid 406 of the *Drosophila* kinesin-1 coiled-coil and fused to a C-terminal His_6 tag. BL21(DE3) strains containing 406-amino acid length constructs were started in a 1-liter LB broth flask overnight, and this seed flask was used to inoculate 20 liters of Terrific Broth plus 100 μg/ml ampicillin in a Micros 30 L or Mobile Pilot Plant 80 L fermentor housed at the Pennsylvania State University Huck Life Sciences Institute Shared Fermentation Facility. After growing to 5–7 OD, expression was induced by the addition of 1 mM isopropyl 1-thio-β-D-galactopyranoside. After overnight expression at 18 °C, bacteria were pelleted using a Sharples T-1-P or AS-16 centrifugation system. Bacterial paste was frozen at −80 °C for later use. Following nickel column purification, motors were exchanged into 25A200 buffer (25 mM K-ACES, pH 6.9, 2 mM magnesium acetate, 2 mM K-EGTA, 0.1 mM K_2-EDTA, 1 mM β-mercaptoethanol, 200 mM KCl) containing either 10 μM ATP or 0.5 μM mADP using an AKTA FPLC system with GE HiTrap desalting column. For storage, 10% (w/v) sucrose was added to all motor solutions, samples were frozen on liquid N_2 and stored at −80 °C. Final motor dilutions were 1:100 or greater, and the small contribution of KCl in final buffer (2 mM or less) was ignored. A subset of the motors was exchanged into mADP by incubating motors in elution buffer (which contains 10 μM ADP) with 100 μM mADP and then exchanging into 25A200 plus 0.5 μM mADP. The concentration of active motors was measured by adding 1 mM ADP to a motor sample to chase off bound mADP, measuring the total mADP concentration (356-nm excitation/450-nm emission) in a Shimadzu 3000 spectrofluorometer, and subtracting the contribution of the 0.5 μM free mADP in the buffer. Stock motor concentrations were in the range of 1–30 μM dimer. Unless otherwise specified, for stopped-flow experiments using mADP-bound motors, motors were diluted without adding additional mADP. GFP-labeled motors were quantified by GFP absorption at 488 nm using $\epsilon_{488} = 55{,}000\ \mathrm{M}^{-1}\ \mathrm{cm}^{-1}$. All experiments were carried out in BRB80 buffer (80 mM PIPES, 1 mM EGTA, 1 mM $MgCl_2$, pH 6.8) to allow for direct comparison of rates.

ATPase Assays—ATPase was quantified by an enzyme-coupled assay following a protocol modified from Huang and Hackney (30). BRB80 buffer was supplemented with 1 mM MgATP, 2 mM phosphoenolpyruvate, 1 mM $MgCl_2$, 0.2 mg/ml casein, 10 μM Taxol, 0.25 mM NADH, and [1.5/100] volume of PK/LDH (Sigma P-0294). Motor concentrations between 10 and 50 nM were used, and absorbance at 340 nm was recorded on an Agilent 9453A UV-visible spectrophotometer. Rates were estimated by linear fit to regions of steady-state absorbance decrease.

Microtubule Pelleting Assays—Pelleting assays were carried out in BRB80 supplemented with 1 mM $MgCl_2$, 10 μM Taxol, 1 mg/ml casein, and 1 mg/ml BSA plus added nucleotide. Mt and GFP-labeled motors were incubated for 10 min with 1 mM MgADP or 2 mM MgATP, whereas the control group was incubated in 1 mM MgAMPPNP. Samples were then centrifuged for 10 min in a Beckman-Coulter Airfuge A-100/18 rotor to pellet microtubules with bound motors. For the ATP experiments, incubation was kept to a maximum of 5 min to minimize ATP depletion, and an ATP regeneration system consisting of 1 μg/ml creatine phosphokinase and 2 mM phosphocreatine was added. GFP fluorescence (488-nm excitation/512-nm emission) was used to quantify motor concentrations in the prespin and supernatants, and the fraction of pelleted motors was calculated. Pelleting data are presented relative to the amount pelleted in AMPPNP.

mADP-ADP Competition Assays—mADP-ADP competition and nucleotide release assays were carried out by spectrofluo-

rometer (356-nm excitation/450-nm emission). For competition assays, 0.4 μM motors were incubated with 2 μM Mt and 2 μM mADP and titrated against varying concentrations of unlabeled ADP. The IC_{50}, defined as the [ADP] where the fluorescence signal drops to 50%, was fit using Morrison's quadratic equation (31),

$$\frac{F_I}{F_0} = \frac{[K] - [ADP] - IC_{50} + \sqrt{([K] + [ADP] + IC_{50})^2 - 4[K]IC_{50}}}{2[K]} \quad \text{(Eq. 1)}$$

where F_I and F_0 are fluorescence in the presence and absence, respectively, of added ADP, and [K] is the total motor concentration. From the IC_{50}, the relationship between the equilibrium binding constants for mADP and ADP was obtained using the Cheng-Prusoff equation (32),

$$K_D^{ADP} = \frac{IC_{50}}{1 + \frac{[mADP]}{K_D^{mADP}}} \quad \text{(Eq. 2)}$$

which for $[mADP] \gg K_D^{mADP}$ simplifies to the following.

$$IC_{50} = \frac{K_D^{ADP}}{K_D^{mADP}}[mADP] \quad \text{(Eq. 3)}$$

Single-molecule Fluorescence—Single-molecule imaging of GFP-labeled motors was carried out using a TIRF microscope at room temperature, as described previously (18). Microtubules were polymerized using a 1:20 ratio of Cy5-labeled (GE Healthcare) and unlabeled tubulin and were surface-immobilized by a monoclonal anti-β-tubulin antibody (Sigma T7816), followed by blocking with 0.5 mg/ml casein + 1 mg/ml BSA. Binding events were scored manually, and dwell time and run length histograms were fit by single exponential distributions. Motor off-rates in ADP were fit using the following scheme.

$$K_{\langle\phi\rangle}Mt + ADP \underset{k_{off}^{ADP}}{\overset{k_{on}^{ADP}}{\rightleftharpoons}} K_{(ADP)}Mt \xrightarrow{k_{unbind}} K_{(ADP)} + Mt$$

SCHEME 1

The mean residence time on the microtubule was calculated based on the mean residence time in the apo- and ADP-states (33), respectively,

$$\tau_D = \frac{1}{k_{off}^{ADP} + k_{unbind}} \quad \text{(Eq. 4)}$$

$$\tau_\phi = \frac{1}{k_{on}^{ADP}[ADP]} \quad \text{(Eq. 5)}$$

and the transition probabilities between states,

$$P_{D\to\phi} = \frac{k_{off}^{ADP}}{k_{off}^{ADP} + k_{unbind}} = k_{off}^{ADP}\tau_D \quad \text{(Eq. 6)}$$

$$P_{\phi\to D} = 1 \quad \text{(Eq. 7)}$$

The mean dwell time on the microtubule, T, is as follows,

$$T = \tau_D + P_{D\to\phi}(\tau_\phi + P_{\phi\to D}T) \quad \text{(Eq. 8)}$$

or

$$T = \frac{\tau_D + P_{D\to\phi}\tau_\phi}{1 - P_{D\to\phi}P_{\phi\to D}} = \frac{k_{on}^{ADP}[ADP] + k_{off}^{ADP}}{k_{unbind}k_{on}^{ADP}[ADP]} \quad \text{(Eq. 9)}$$

The observed off-rate, k_{obs}, is equal to the reciprocal of the mean dwell time,

$$k_{obs} = \frac{1}{T} = \frac{k_{unbind}[ADP]}{[ADP] + K_D^{ADP}} \quad \text{(Eq. 10)}$$

where

$$K_D^{ADP} = \frac{k_{off}^{ADP}}{k_{on}^{ADP}} \quad \text{(Eq. 11)}$$

Steady-state Motility Assays—Gliding assays were carried out as described previously (34). Motors were attached to the surface through a monoclonal anti-His antibody (Invitrogen, catalog no. 1046237), and velocities were quantified with the MtrackJ plug-in in ImageJ (National Institutes of Health).

Stopped-flow Setup—All stopped-flow experiments were carried out on an Applied Physics SX20 spectrofluorometer using 356-nm excitation with an HQ480SP emission filter. All assays were carried out in BRB80 buffer supplemented with 1 mM $MgCl_2$ and 5 μM Taxol.

k_{on}^{Mt} Experiment—Motors were first incubated with 0.5 μM mADP to exchange the ADP in the head domain. 0.1 μM motors were mixed against varying concentration of Mt with 1 mM ADP. The data were fit to a biexponential, and the fast phase was fit to the following equation to obtain the maximal mADP off-rate and apparent Mt affinity.

$$k_{obs} = \frac{k_{off}^{mADP}[Mt]}{[Mt] + K_{0.5}^{Mt}} + c \quad \text{(Eq. 12)}$$

Half-site Experiment—Motors were combined with microtubules to generate a species with one head bound and mADP in the tethered head. This complex was then flushed against a solution containing ATP or AMPPNP, the data were fit by a biexponential, and the faster rates were fit to the following equation to obtain the maximum half-site release rate and apparent nucleotide binding affinity.

$$k_{obs} = \frac{k_{max}^{ATP/HS}[ATP]}{[ATP] + K_{0.5}^{ATP/HS}} \quad \text{(Eq. 13)}$$

Unstrained and Strained Nucleotide Exchange Kinetics—0.1–0.2 μM motors were combined with 20-fold Mt to generate a species with one head bound and mADP in the tethered head. To generate a two-head-bound species, an additional 200 μM AMPPNP was added. These complexes were flushed against varying mant-nucleotide concentrations (*mAxP*), the data were fit by a biexponential, and the faster rates were fit by linear regression to obtain the nucleotide on- and off-rates.

$$k_{obs} = k_{on}^{mAxP}[mAxP] + k_{off}^{mAxP} \quad \text{(Eq. 14)}$$

Model for Sequential Release—The sequential release experiment in Fig. 4*d* was modeled using the following scheme.

$$K(\text{mADP})_2 \xrightarrow{k_1} K(\text{mADP})_1 \xrightarrow{k_2} K(\text{mADP})_0$$

SCHEME 2

In the first step, microtubule binding triggers release of one mADP, and in the second step, ATP binding triggers stepping and release of the second mADP. The observed rates for the two mADP release steps are as follows.

$$k^1_{\text{obs}} = k_1 \quad \text{(Eq. 15)}$$

$$k^2_{\text{obs}} = \frac{1}{1/k_1 + 1/k_2} = \frac{k_1 k_2}{k_1 + k_2} \quad \text{(Eq. 16)}$$

When the rates of the first and second steps are similar, the observed rate for the total signal drop, k_{obs}, can be approximated as follows.

$$k_{\text{obs}} \cong \frac{1}{2}(k^1_{\text{obs}} + k^2_{\text{obs}}) = \frac{1}{2}\left(k_1 + \frac{k_1 k_2}{k_1 + k_2}\right) \quad \text{(Eq. 17)}$$

These modeled rates are compared with the experimental rates in Fig. 4*d*. To estimate errors, the equation was linearized by Taylor series expansion,

$$k_{\text{obs}} = \overline{k_{\text{obs}}} + \frac{\partial k_{\text{obs}}}{\partial k_1}k_1 + \frac{\partial k_{\text{obs}}}{\partial k_2}k_2 + \cdots \quad \text{(Eq. 18)}$$

where $\overline{k_{\text{obs}}}$ is the mean rate, and higher order terms are ignored. The slope for the first-order approximation can be calculated as follows.

$$\frac{\partial k_{\text{obs}}}{\partial k_1} = \frac{1}{2}\left(1 + \left(\frac{k_2}{k_1 + k_2}\right)^2\right) \quad \text{(Eq. 19)}$$

$$\frac{\partial k_{\text{obs}}}{\partial k_2} = \frac{1}{2}\left(1 + \left(\frac{k_1}{k_1 + k_2}\right)^2\right) \quad \text{(Eq. 20)}$$

Thus, the S.E. of k_{obs} is the following,

$$se_{\text{obs}} \cong \sqrt{\left(\frac{\partial k_{\text{obs}}}{\partial k_1}\right)^2 se_1^2 + \left(\frac{\partial k_{\text{obs}}}{\partial k_2}\right)^2 se_2^2} \quad \text{(Eq. 21)}$$

where se_1 and se_2 are the experimental S.E. of k_1 and k_2, respectively.

Ensemble Kinetics Simulations—Following determination of the rate constants in Table 2, stopped-flow experiments were simulated by ensemble kinetics simulations, as follows. Free nucleotide concentrations in solution were assumed to be constant, and bimolecular rate constants for nucleotide binding were converted to first order rates by multiplying by the relevant free nucleotide concentrations. For a model with n states (where $n = 8$ in Fig. 1), an n-by-n rate matrix, $\boldsymbol{R}$, was defined, where each element R_{ij} corresponds to the rate constant from state i to j (in s^{-1}). A one-dimensional concentration matrix, $\boldsymbol{c}$, was defined and populated with initial concentrations of every state, $\boldsymbol{c_0}$. The scalar form of the governing equation for any state i is as follows,

$$\frac{d}{dt}c_i = \sum_j R_{ji}c_j - c_i\sum_j R_{ij} \quad \text{(Eq. 22)}$$

and the vector form is as follows.

$$\frac{d}{dt}\boldsymbol{c} = \{\boldsymbol{R}^T - \text{diag}(\boldsymbol{R}\cdot\boldsymbol{1})\}\cdot\boldsymbol{c} \quad \text{(Eq. 23)}$$

We simulated this governing equation using the *ode45* function in MATLAB to produce the concentration matrix $\boldsymbol{C}_{m\times n}$, corresponding to n states at m time points. Each state is assigned a weight, $\boldsymbol{w}_{n\times 1}$, based on the number of bound mant-nucleotides (0, 1, or 2), and the final observed signal, $\boldsymbol{s}_{m\times 1}$, is the sum of the signal contributions from each state.

$$\boldsymbol{s} = \boldsymbol{C}\cdot\boldsymbol{w} \quad \text{(Eq. 24)}$$

To simulate different stopped-flow experiments, different matrices were defined based on specific experimental parameters, and simulated fluorescence traces were obtained for each. Traces were fit by single- or biexponential functions in Origin version 9.1 and compared with the experimental data (Fig. 9, *d–j*). MATLAB code can be found in the supplemental material as EnsembleKineticsSimulation.m.

Single-molecule Simulations—Single-molecule simulations in Fig. 9, *a*–c, were carried out using the rate matrix $\boldsymbol{R}$, defined above, using an approach used previously (18, 28) but executed in a different manner. The mean dwell time in every state, i, is as follows,

$$t_i = \frac{1}{\sum_j R_{ij}} \quad \text{(Eq. 25)}$$

where R_{ij} are the rate constants out of state i. The dwell time matrix is defined as follows.

$$\boldsymbol{t} = \text{diag}(\boldsymbol{R}\cdot\boldsymbol{1})^{-1}\cdot\boldsymbol{1} \quad \text{(Eq. 26)}$$

Because all rate constants are first order, the dwell time in a given state i follows an exponential distribution with mean dwell time t_i. The distributions of dwell times for every state were obtained using the Gillespie algorithm (28, 35).

When transitioning out of state i, the probability of transitioning to any state j is as follows.

$$P_{ij} = \frac{R_{ij}}{\sum_j R_{ij}} = R_{ij}t_i \quad \text{(Eq. 27)}$$

The transition rates and dwell times were used to define the transition probability matrix.

$$\boldsymbol{P} = \text{diag}(\boldsymbol{t})\cdot\boldsymbol{R} \quad \text{(Eq. 28)}$$

The probability of transitioning from state i to any state j is determined by the ith row of the transition probability matrix, where the sum of every row equals 1. The new state, j, was chosen by selecting a random number from a uniform distribution from 0 to 1 and choosing the transition based on the relative probabilities, P_{ij}.

Simulations recorded the run duration, run length, and dis-

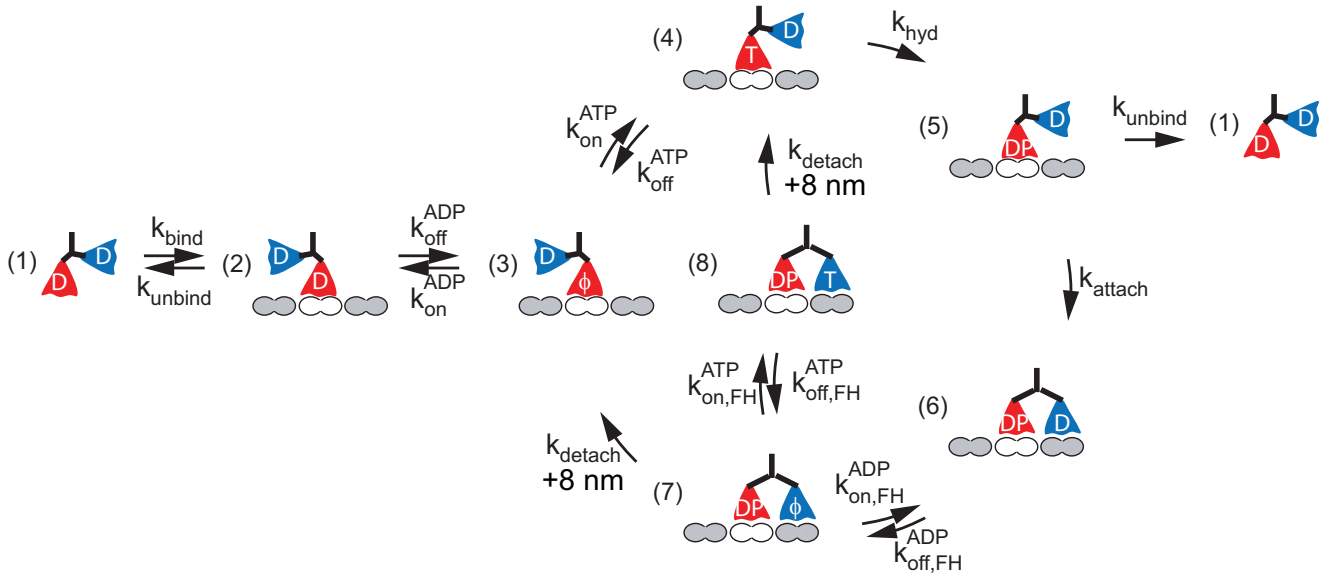

FIGURE 1. **Model for the KIF3A chemomechanical cycle.** Motors in solution (*state 1*) bind to the Mt (*state 2*), triggering ADP release (*state 3*). Next, ATP binds (*state 4*) and is hydrolyzed (*state 5*), and the tethered head binds (*state 6*) and releases its ADP, generating a two-head-bound state (*state 7*). If nucleotide binding to the front head is gated, then the rear head detaches to complete the cycle (*state 3*). If front head gating is not present, then ATP can bind before the trailing head detaches (*state 8*), which could potentially lead to hydrolysis and premature unbinding (not shown). Front head gating is defined as $k_{on,FH}^{ATP} < k_{on}^{ATP}$, and rear head gating is defined as $k_{detach} > k_{unbind}$. Note that detachment from state 5 may involve P_i release followed by detachment from the ADP state. See "Results" for further details, and see Table 2 for KIF3A rate constants.

tribution of step times for each of 1000 motors. Motor velocity was calculated by dividing the run length by the run duration, and the randomness parameter was estimated from the distribution of step durations (33, 36). MATLAB code can be found in the supplemental material as SingleMoleculeSimulation.m.

Gliding Assay Simulations—Steady-state gliding velocities were simulated by calculating the expected time for a motor to complete one entire hydrolysis cycle, following the approach of Moffitt *et al.* (33). State 6 was assigned as the starting point because it does not have a bifurcation. To avoid a singularity of our final solution, we created a phantom state 6′ as the destination, resulting in a new rate matrix, $\boldsymbol{R}'$, having an extra dimension. The transitions into state 6 were replaced by transitions into state 6′, and the transition rates into state 6 and out of state 6′ were set to zero. To model the high local [Mt] for motors in the gliding assay, [Mt] was set to 1000 μM.

As with the single-molecule simulations, a dwell time matrix, $\boldsymbol{t}_{n\times 1}$, was defined, with each element (other than the terminal state 6′) calculated as follows.

$$t_i = \frac{1}{\sum_{j=1}^{n+1} R'_{ij}} \qquad \text{(Eq. 29)}$$

Next, starting from the state transition probability matrix, a new matrix, $\boldsymbol{M}_{n\times n}$ was created by omitting state 6′.

$$M_{ij} = R'_{ij} t_i \qquad \text{(Eq. 30)}$$

Finally, a new matrix, $\boldsymbol{T}$, was created that defines the mean time from each state, i, to the terminal state 6′,

$$\boldsymbol{T} = \boldsymbol{M} \cdot \boldsymbol{T} + \boldsymbol{t} \qquad \text{(Eq. 31)}$$

whose solution is as follows.

$$\boldsymbol{T} = (\boldsymbol{I} - \boldsymbol{M})^{-1} \cdot \boldsymbol{t} \qquad \text{(Eq. 32)}$$

The stepping velocity, calculated as the reciprocal of the run time starting at state 6,

$$v = \frac{1}{T_6} \qquad \text{(Eq. 33)}$$

was compared with the experimental gliding velocities in Fig. 9, *k* and *l*. MATLAB code can be found in the supplemental material as GlidingAssaySimulation.m.

Data Analysis—Curve fitting was carried out using nonlinear regression in Origin version 9.1 software. For fits, data points were weighted by the inverse of their S.E.

RESULTS

Conceptual Hydrolysis Model of KIF3A—To reveal differences between the hydrolysis cycle of kinesin-2 and kinesin-1, we used a KIF3 homodimeric construct (KIF3A/A) containing the head and neck linker of *M. musculus* KIF3A linked to the coiled-coil of *Drosophila* kinesin-1. Its velocity, run length, and load-dependent properties have been shown to match those of full-length KIF3A/B (18, 28, 29). Here, KHC denotes conventional kinesin, which has a 14-residue neck linker domain. $KIF3A_{17}$ denotes the KIF3A/A homodimer having the wild-type 17-residue neck linker domain, and $KIF3A_{14}$ denotes the same motor with a Pro-Ala swap and deletion of the last three residues in the neck linker to match that of KHC (18).

As a starting point for analysis of the KIF3A hydrolysis cycle, we started from a hydrolysis cycle developed for kinesin-1 (Fig. 1) (18, 28). The cycle begins with motors in solution having an ADP bound to each head (state 1) (37). The initial interaction of the motor with the microtubule lattice is a weak binding state (state 2) that converts to a strongly bound state following ADP release (state 3) (12, 38–40). Binding of ATP (state 4) triggers neck linker docking and ATP hydrolysis (state 5) (41), which is

followed by microtubule binding (state 6) and ADP release by the tethered head (state 7) (12, 42). In this scheme, processivity is determined by the race between binding of the tethered head to the next binding site (state 5 to 6) and dissociation of the bound head from the microtubule (state 5 to 1). From state 7, intramolecular strain in the two-head-bound conformation accelerates rear head detachment (state 3), completing the hydrolysis cycle and resulting in one 8-nm step. Front head gating is incorporated into this scheme by postulating that ATP binding to the leading head in state 7 is inhibited due to rearward strain, preventing premature hydrolysis and detachment (24). Rear head gating is incorporated by the fact that dissociation from the one-head-bound state 5 is slower than detachment of the trailing head in the two-head-bound state 7 (20). To understand the KIF3A hydrolysis cycle, experiments were designed to measure each parameter in Fig. 1.

In the ADP State, KIF3A Binds Microtubules More Strongly than Kinesin-1—To unravel the hydrolysis cycle, we first measured the steady-state ATPase of KIF3A and kinesin-1 (Fig. 2*a*). The motors had similar $K_{0.5}^{Mt}$ (KIF3A-GFP: 1.0 ± 0.2 μM Mt; KHC-GFP: 1.9 ± 0.4 μM Mt), indicating similar microtubule affinities when the motors were actively stepping along microtubules and hydrolyzing ATP. This similarity in $K_{0.5}^{Mt}$ for ATPase is consistent with previous single-molecule motility experiments that found that kinesin-2 and kinesin-1 had similar dwell times on the microtubule in saturating ATP (18).

Next, microtubule pelleting assays were carried out to compare microtubule affinities of the motors in different nucleotide states. The dissociation rate from the ADP-P_i state (*state 5* in Fig. 1) is of particular interest for understanding processivity, but due to the difficulty in reversing P_i release by adding free P_i to solution (43), we used the ADP state (*state 2* in Fig. 1) as a proxy for the ADP-P_i state. In monomeric rat kinesin-1, the microtubule affinity in the ADP state was found to be elevated in the presence of added P_i (44), but subsequent work suggested that the effect may be caused by inhibition of ADP binding by P_i (43); there is no evidence that the ADP-P_i state has a lower affinity than the ADP state.

Surprisingly, in the ADP state, KIF3A had a nearly 20-fold higher Mt affinity than KHC (K_D^{Mt} of 0.45 ± 0.07 μM Mt for KIF3A-GFP and 11 ± 0.3 μM Mt for KHC-GFP; Fig. 2*b*). To rule out the possibility that this high affinity for KIF3A resulted from both heads binding to the microtubule in ADP due to its longer neck linker domain, the experiment was repeated with $KIF3A_{12}$, which was previously shown to be a non-processive motor due to its shortened neck linker (27). K_D^{Mt} for $KIF3A_{12}$ was 0.61 ± 0.07 μM Mt (data not shown), indicating that this affinity was a property of the motor domains alone.

This high microtubule affinity of $KIF3A_{17}$ in ADP contrasts with previous single-molecule run length measurements that found that $KIF3A_{17}$ is 4-fold less processive than KHC (18). There are two possible resolutions to this paradox: (i) KIF3A detaches in a different nucleotide state than kinesin-1, or (ii) KIF3A spends a larger fraction of its hydrolysis cycle in the weak binding state. To test the first hypothesis, we carried out Mt pelleting assays in different nucleotides. In both AMPPNP, which mimics the ATP-bound state, and the absence of nucleotide, KIF3A bound tightly to microtubules (Fig. 2*c*), consistent with previous results from kinesin-1. In ATP, the K_D^{Mt} was 0.62 ± 0.08 μM Mt, confirming the ATPase results (Fig. 2*d*). Thus, we conclude that during its normal hydrolysis cycle, KIF3A does not detach from these high affinity states (states 3, 4, 6, and 7 in Fig. 1). The finding that the K_D^{Mt} for Mt in ADP matches both the $K_{0.5}^{Mt}$ and K_D^{Mt} in ATP implies that KIF3A spends a large fraction of its hydrolysis cycle in a weak binding state (*state 5* in Fig. 1).

To better understand the high Mt affinity of KIF3A in the ADP state, we directly measured the microtubule binding and unbinding rates using stopped-flow and single-molecule fluorescence experiments, respectively. At low microtubule concentrations, release of mADP from the motor is limited by microtubule binding. Thus, to measure the on-rate for microtubule binding, motors loaded with mADP were flushed against varying concentrations of microtubules, and the bimolecular on-rate was obtained by fitting the slope (Fig. 2*e*). The linear relationship demonstrates the pseudo-first-order [Mt] binding step, with k_{bind} = 3.1 ± 0.1 $\mu M^{-1}\ s^{-1}$. To measure the microtubule unbinding rate, single-molecule TIRF experiments were used to measure the distribution of dwell times of KIF3A-GFP motors binding to surface-immobilized microtubules in varying concentrations of ADP (Fig. 2*f*). At saturating ADP, the motor unbinding rate was k_{unbind} = 2.1 ± 0.2 s^{-1}, giving an estimate for the K_D^{Mt} (where $K_D^{Mt} = k_{unbind}/k_{bind}$) of 0.68 μM. This K_D^{Mt} calculated from stopped-flow and single-molecule measurements matches the K_D^{Mt} from pelleting assays in ADP (0.45 μM; Fig. 2*b*), confirming this relatively high microtubule affinity of KIF3A in ADP.

The k_{cat} of 42 s^{-1} from the ATPase measurement in Fig. 2*a* (which also agrees with the gliding velocity of 47 s^{-1} in Fig. 9*l*) sets a lower limit for rear head detachment rate during stepping. The 2.1 s^{-1} unstrained motor unbinding rate in ADP (Fig. 2*f*) is 20-fold slower than this. Thus, rear head gating (detachment of the rear head is accelerated by binding of the leading head in the two-head-bound state) is present in the KIF3A hydrolysis cycle. The next series of experiments were designed to assess front head gating, starting with characterization of mant-nucleotides as substrates for dimeric KIF3A and progressing to measurements of nucleotide exchange kinetics under different conditions.

Mant-nucleotides Are Competent Substrates for KIF3A and Bind More Tightly than Unlabeled Nucleotide—mATP has been shown to be a suitable analog of ATP for a number of kinesins and is widely employed in stopped-flow studies due to its fluorescence enhancement upon motor binding (38, 39, 45, 46). However, other enzymes, including myosin, have been shown to have higher affinity for mant-nucleotides than unlabeled nucleotides, which has been attributed to stabilizing hydrophobic interactions between the mant-moiety and residues in the nucleotide binding pocket (47–50). To compare the affinity of KIF3A for mADP *versus* unlabeled ADP, we carried out mADP-ADP competition assays to quantify the ratio of equilibrium constants K_D^{mADP}/K_D^{ADP} (Fig. 3*a*). The IC_{50} was obtained by titrating ADP against KIF3A incubated in mADP and measuring the change in fluorescence due to mADP unbinding. The IC_{50} was measured to be 25.4 ± 1.1 μM ADP in

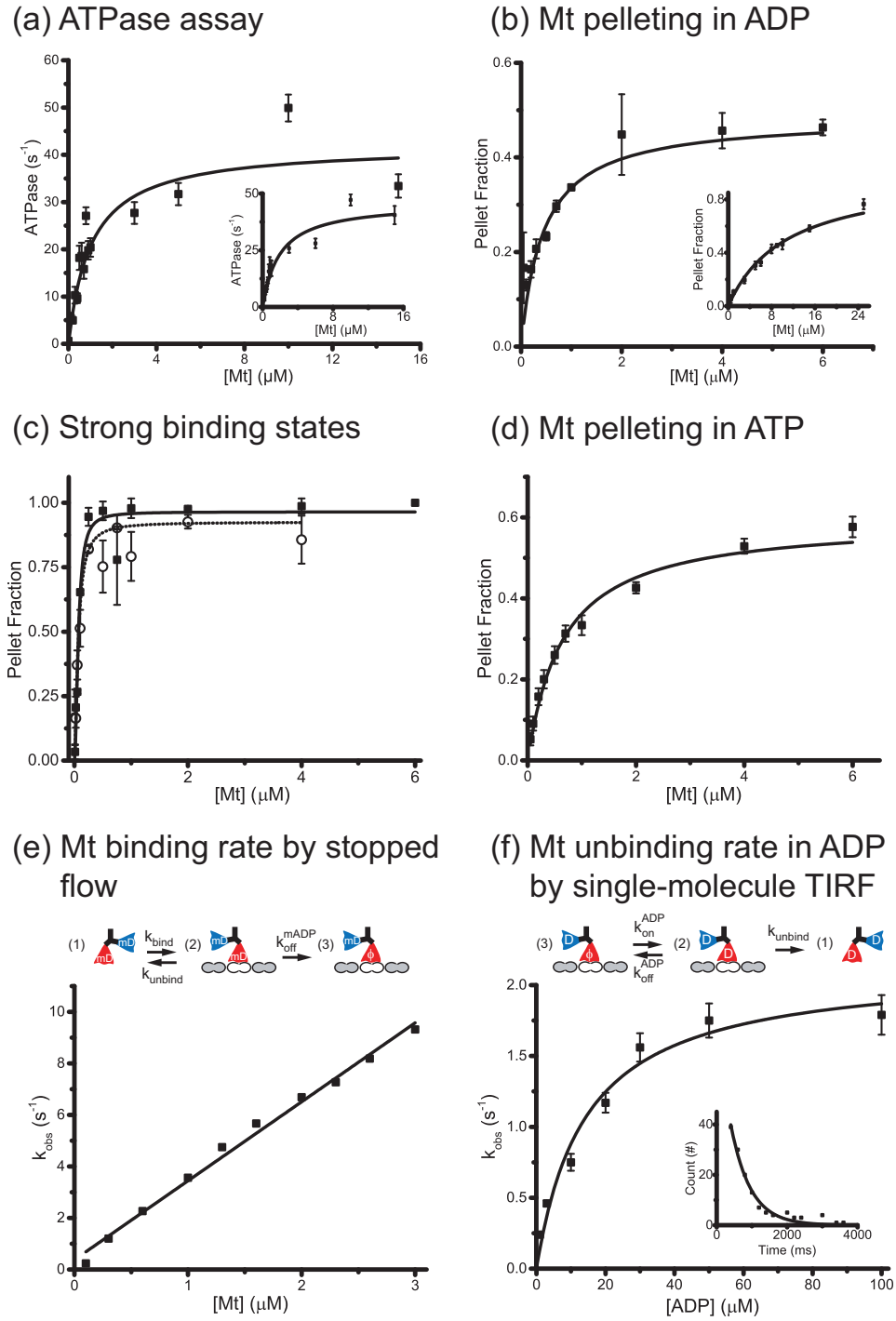

FIGURE 2. **KIF3A microtubule affinity determination.** *a*, Mt-stimulated ATPase activity of KIF3A$_{17}$-GFP. From Michaelis-Menten fit, $k_{cat} = 42 \pm 4\ s^{-1}$ and $K_{0.5}^{Mt} = 1.0 \pm 0.2\ \mu M$ Mt. *Inset*, ATPase of KHC-GFP with $K_{0.5}^{Mt} = 1.9 \pm 0.4\ \mu M$ Mt and $k_{cat} = 46 \pm 4\ s^{-1}$. Data are mean ± S.D. (*error bars*) from three independent determinations at each [Mt]. *b*, Mt affinity of KIF3A$_{17}$-GFP in 1 mM ADP from the pelleting assay. Hyperbolic fit gave K_D^{Mt} of 0.45 ± 0.07 μM Mt and maximum pellet of 0.49 ± 0.03. Data are mean ± S.D. (*error bars*) from three independent determinations at each [Mt]. *Inset*, Mt affinity of KHC-GFP in 1 mM ADP, giving K_D^{Mt} of 11 ± 0.3 μM Mt. *c*, Mt affinity of KIF3A$_{17}$-GFP in 1 mM AMPPNP and no added nucleotide, giving K_D^{Mt} of 0.056 ± 0.012 and 0.039 ± 0.006 μM Mt, respectively. *d*, Mt affinity of KIF3A$_{17}$-GFP in 2 mM ATP plus regenerating system, giving K_D^{Mt} of 0.62 ± 0.08 μM Mt. The finding that the binding isotherms extrapolate to less than 1.0 suggests that there may be a subpopulation of motors that pellet in AMPPNP but do not pellet in ADP or ATP. *e*, Mt binding rate for KIF3A$_{17}$-GFP. A schematic describes the portion of the hydrolysis cycle being interrogated. KIF3A$_{17}$ motors were flushed against varying [Mt], and traces (average of $n = 5$ at each [Mt]) were fit with a rising exponential with rate constant k_{obs}. Linear fit to k_{obs} at low [Mt] gave the microtubule binding rate, $k_{bind} = 3.1 \pm 0.1\ \mu M^{-1}\ s^{-1}$. *f*, Mt unbinding rate for KIF3A$_{17}$-GFP. Single-molecule dwell time measurements in varying [ADP] give a maximal detachment rate, $k_{unbind} = 2.1 \pm 0.2\ s^{-1}$ and K_D^{ADP} of 14 ± 3 μM ADP ($n > 130$ events at each [ADP]). *Inset*, distribution of KIF3A$_{17}$-GFP dwell times at 100 μM ADP ($n = 165$).

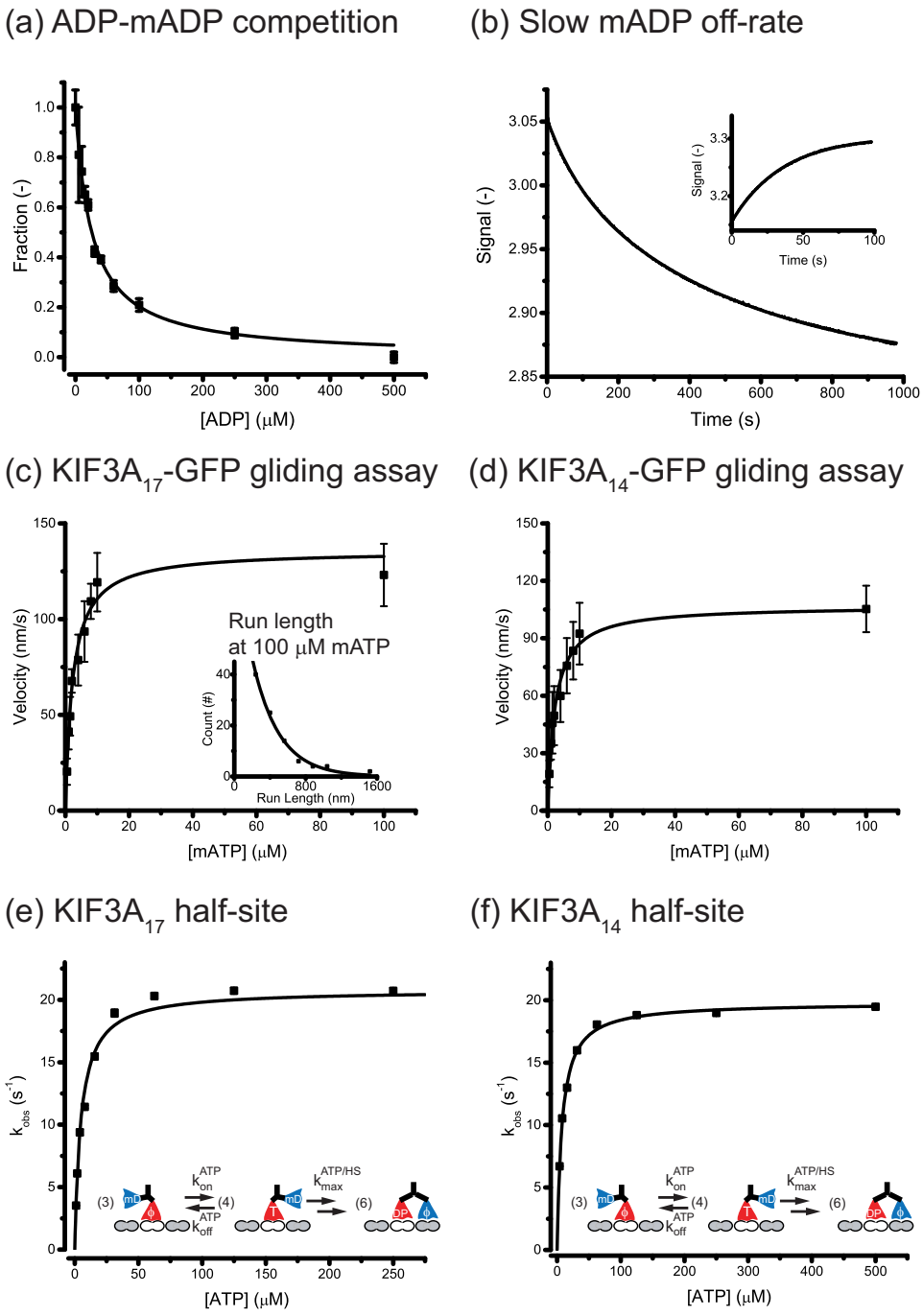

FIGURE 3. **KIF3A binds mADP more strongly than unlabeled ADP.** *a*, competition experiment to determine relative affinities of ADP and mADP. Relative steady-state fluorescence is plotted for different concentrations of ADP added to a solution of 0.4 μM dimeric KIF3A$_{17}$ plus 2 μM Mt and 2 μM mADP. A fit to the Morrison quadratic curve (see "Experimental Procedures") gave IC_{50} of 25.4 $\pm$ 1.1 μM ADP, suggesting a 13-fold higher affinity of KIF3A for mADP than unlabeled ADP. Data are mean $\pm$ S.D. (*error bars*) from three independent determinations at each [ADP]. *b*, mADP off-rate determination. 0.5 μM KIF3A$_{17}$ in 0.5 μM mADP was flushed against 1 mM ADP and the fall in fluorescence ($n = 5$) resulting from mADP unbinding fit by a biexponential having a dominant slow rate constant of 0.0019 $\pm$ 0.000015 s^{-1}, which is interpreted as the mADP dissociation rate. The faster component with a rate of 0.011 $\pm$ 0.0002 s^{-1} and relative amplitude of ~0.25 was attributed to mant-isomerization, which was characterized previously to be 0.01–0.04 s^{-1} (46). *Inset*, unlabeled ADP off-rate, determined by flushing 0.5 μM KIF3A$_{17}$ plus 0.5 μM ADP against 10 μM mADP and monitoring the fluorescence increase due to mADP binding (rate limited by ADP dissociation). Fitting a single exponential gave a rate constant 0.028 $\pm$ 0.000048 s^{-1} for ADP dissociation ($n = 5$). *c*, gliding assays (total 374 events) of KIF3A$_{17}$-GFP in varying [mATP] giving $k_{step}^{mATP} = 17.0 \pm 0.8$ s^{-1} and $K_m^{mATP} = 2.3 \pm 0.3$ μM. *d*, gliding assays (total 155 events) of KIF3A$_{14}$-GFP in varying [mATP] giving $k_{step}^{mATP} = 13.4 \pm 0.4$ s^{-1} and $K_m^{mATP} = 2.3 \pm 0.2$ μM. Velocities in unlabeled ATP were 47 s^{-1} for KIF3A-GFP and 43 s^{-1} for KIF3A$_{14}$-GFP (data not shown). *e*, half-site nucleotide release experiment for KIF3A$_{17}$, determined by flushing 0.1 μM motor with 2 μM Mt against varying [ATP]. From a fit to the data, $k_{max}^{ATP/S} = 21 \pm 0.7$ s^{-1} and $K_{0.5}^{ATP/HS} = 5 \pm 0.3$ μM ATP. Data are means $\pm$ S.E. (*error bars*) from exponential fits to averaged transients ($n = 5$–6) at each [ATP]. *f*, half-site nucleotide release experiment for KIF3A$_{14}$, determined by flushing 0.1 μM motor with 2 μM Mt against varying [ATP]. The fit result gives $k_{max}^{ATP/HS} = 20 \pm 0.2$ s^{-1} and $K_{0.5}^{ATP/HS} = 8 \pm 0.2$ μM ATP. Data are means $\pm$ S.E. from an exponential fit of averaged transients ($n = 5$–6) at each [ATP].

the presence of 2 μM mADP, suggesting a 13-fold difference in nucleotide affinities (see "Experimental Procedures").

Next, we measured the kinetics of ADP dissociation from KIF3A in the absence of microtubules. The mADP off-rate, obtained by adding a saturating concentration of unlabeled ADP to a solution of motors incubated in mADP and monitoring the fall in fluorescence, was $0.0019 \pm 0.000015\ s^{-1}$ (Fig. 3*b*). A second process with a faster rate constant ($\sim 0.011\ s^{-1}$) and smaller amplitude ($\sim$20% of the total signal drop) was attributed to mant-isomerization, which has been characterized as $\sim 0.01\ s^{-1}$ in previous studies (46). In contrast, the off-rate of unlabeled ADP, obtained by adding mADP to motors incubated in unlabeled ADP, was $0.028 \pm 0.000048\ s^{-1}$ (Fig. 3*b*, *inset*). The 15-fold difference in off-rates suggests that the mant-moiety contributes stabilizing interactions between the nucleotide and the nucleotide-binding pocket. For KHC, solution off-rates were 0.033 and $0.022\ s^{-1}$ for ADP and mADP, respectively (data not shown), confirming that the slow mADP off-rate for KIF3A was not the result of contaminants in the mADP stock. The agreement between the ratio of off-rates and the ratio of equilibrium constants for KIF3A suggests that on-rates for unlabeled ADP and mADP binding to KIF3A are similar.

To confirm that mATP is a competent substrate for KIF3A, microtubule gliding assays were carried out for $KIF3A_{17}$-GFP and $KIF3A_{14}$-GFP at varying concentrations of mATP (Fig. 3, *c* and *d*). Fitting the velocity data gave an overall stepping rate k_{step}^{mADP} of $17.0 \pm 0.8\ s^{-1}$ for $KIF3A_{17}$, which is 3-fold slower than the $47 \pm 5\ s^{-1}$ measured in unlabeled ATP (Fig. 9*l*). This slowed speed in mATP is consistent with the high mADP affinity measured above and suggests that when mATP is the substrate, mADP release is the rate-limiting step in the hydrolysis cycle. The low K_m^{mADP} of 2.3 ± 0.3 μM for $KIF3A_{17}$ is also consistent with this high mADP affinity. The gliding speed of $KIF3A_{14}$ was slightly slower than $KIF3A_{17}$ (Fig. 3*d*), consistent with previous single-molecule velocities (18). To confirm processivity, run lengths were measured using a single-molecule TIRF assay at 100 μM mATP (Fig. 3*c*, *inset*). The mean run length was 300 ± 20 nm, and the mean dwell time (not shown) was 1.7 ± 0.3 s, confirming that motor processivity is retained in mATP.

To test the hypothesis that the slower gliding speeds in mATP resulted from mADP release being rate-limiting, we carried out half-site release experiments to measure the mADP release rate during KIF3A stepping, as follows. Motors incubated in mADP were combined with microtubules to generate a one-head-bound state (*state 3* in Fig. 1). These complexes were mixed against varying concentrations of ATP in a stopped-flow spectrometer, and the fall in fluorescence due to mADP release was monitored (Fig. 3, *e* and *f*). At low [ATP], the rate is expected to be proportional to the nucleotide concentration, whereas at saturating ATP, the rate will be limited by mADP release. The maximal release rate, $k_{max}^{ATP/HS}$ was 21 ± 0.7 and $20 \pm 0.2\ s^{-1}$ for $KIF3A_{17}$ and $KIF3A_{14}$, respectively, and the ATP concentrations for half-maximal rate $k_{0.5}^{ATP/HS}$ were 5 ± 0.3 and 8 ± 0.2 μM ATP for $KIF3A_{17}$ and $KIF3A_{14}$, respectively. The agreement between the mADP release rate and the stepping rate from gliding assays indicates that mADP release is the rate-limiting step. It should be noted that the off-rate of unlabeled ADP was 15-fold faster than mADP (Fig. 3*b*), whereas the stepping rate in unlabeled ATP was 3-fold faster than in mATP (Figs. 3*c* and 9), indicating that under normal ATP conditions, ADP release is not the rate-limiting step for KIF3A.

mADP Exchange Rates in Unstrained KIF3A Determined by Four Different Assays—The next task toward characterizing the KIF3A hydrolysis cycle was to measure the nucleotide exchange rate of the motor in both the one-head-bound unstrained state (*state 3* in Fig. 1) and the two-head-bound strained state (*state 7* in Fig. 1). The key prediction from the front head gating model is that in the two-head-bound state, nucleotide exchange in the front head will be slowed due to intramolecular strain. The unstrained exchange rate was measured in four ways, which provides confirmation of the rates by independent methods and enables the estimation of other rate constants in the hydrolysis cycle.

In the first approach, termed k_{on}^{Mt} (Fig. 4*a*), mADP-loaded motors were flushed against varying concentrations of microtubules in the presence of saturating ADP. Binding to the microtubule triggers mADP release, resulting in a fluorescence drop, and the excess ADP prevents any rebinding of mADP. The hyperbolic plot in Fig. 4*a* shows the transition of the rate-determining step from microtubule binding at low [Mt] to mADP release at saturating [Mt]. The plateau value indicates that the strain-free mADP release rate is $26 \pm 2.3\ s^{-1}$, which is close to the $21\ s^{-1}$ mADP release rate from the half-site experiments in Fig. 3*c*. The second approach was a nucleotide exchange assay, as follows. Motors in unlabeled ADP were incubated with microtubules and flushed against varying [mADP], resulting in a rise in fluorescence due to reversible mADP binding to the microtubule-bound head. The fitted first-order rate constants, which represent the sum of the forward and reverse mADP binding rates, were analyzed by linear regression (Fig. 4*b*). The slope, representing the mADP on-rate k_{on}^{mADP}, was 18 ± 1.3 μM $mADP^{-1}$ s^{-1}, and the *y* intercept, representing the mADP off-rate k_{off}^{mADP}, was $27 \pm 1.3\ s^{-1}$. This off-rate is in line with that obtained in the k_{on}^{Mt} experiments above.

The third experiment was to use a single-molecule TIRF assay to measure the mADP dependence of the $KIF3A_{17}$-GFP microtubule dissociation rate. Dissociation is expected to be very slow in the absence of nucleotide and rise to an observable rate at saturating mADP concentrations, with the mADP affinity of the microtubule-bound motor determining where the transition occurs. Dwell time histograms were fit by exponential distributions to obtain microtubule unbinding rates (Fig. 4*c*, *inset*), and the off-rates as a function of mADP concentration were fit by a hyperbola, giving a maximal off-rate $k_{unbind} = 1.44 \pm 0.09\ s^{-1}$ and an apparent $K_D^{mADP} = 1.8 \pm 0.2$ μM mADP.

The fourth and final method to measure the unstrained mADP exchange rate was a sequential release experiment, in which mADP-loaded motors were flushed against varying concentrations of microtubules in the presence of ATP. In this configuration, the first mADP release is determined by microtubule binding, whereas the second mADP release is determined by the subsequent binding of ATP and stepping of the motor (Fig. 4*d*). Thus, the experiment consists of a k_{on}^{Mt} experiment (Fig. 4*a*) followed by a half-site experiment (Fig. 3*e*) and serves as a check of consistency. At sufficiently high ATP con-

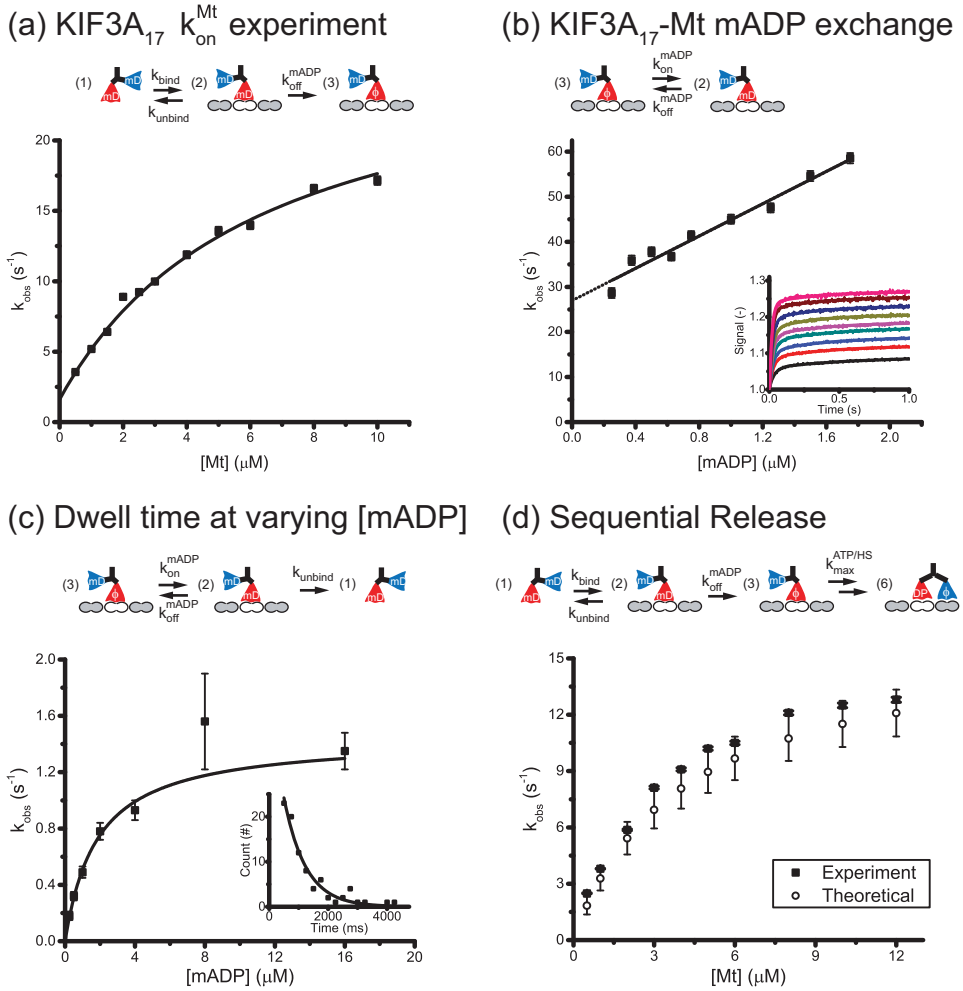

FIGURE 4. **mADP exchange rates in the unstrained Mt-bound head of KIF3A.** *a*, microtubule-stimulated mADP release. $KIF3A_{17}$ incubated in mADP was flushed against varying [Mt] with 500 μM ADP added to prevent mADP rebinding. Averaged transients ($n = 5–6$) were fit with a biexponential, and the fast rate constant was plotted as a function of [Mt]. From the hyperbolic fit (see "Experimental Procedures"), the maximum mADP off-rate was $k_{off}^{mADP} = 26 \pm 2.3\ s^{-1}$ and $K_{0.5}^{Mt} = 6 \pm 1\ \mu$M Mt. A slower process (maximum $\sim 2\ s^{-1}$) with smaller amplitude ($<1/6$) also displayed [Mt] dependence, consistent with it resulting from motor dissociation and reassociation kinetics in ADP. *b*, mADP exchange rates for the motor-Mt complex. 0.1 μM $KIF3A_{17}$ with 2 μM Mt were flushed against varying concentrations of mADP, and the rise in fluorescence was monitored. Observed rates at low [mADP] were fit to the equation, $k_{obs} = k_{on}^{mADP}[mADP] + k_{off}^{mADP}$, giving $k_{on}^{mADP} = 18 \pm 1.3\ \mu M\ mADP^{-1}\ s^{-1}$ and $k_{off}^{mADP} = 27 \pm 1.3\ s^{-1}$. *Inset*, raw traces at varying [mADP] (average of $n = 15–17$/[mADP]) and fits. *c*, single-molecule dwell times of $KIF3A_{17}$-GFP on microtubules at varying [mADP]. A fit to the data (see "Experimental Procedures") gave $k_{off}^{mADP} = 1.44 \pm 0.09\ s^{-1}$ and $K_{0.5}^{Mt} = 1.8 \pm 0.2\ \mu$M mADP ($n > 67$ events for each [mADP]). *Error bars*, S.E. of the fit. *Inset*, dwell time distribution at 16 μM mADP ($n = 114$). *d*, sequential release experiment. 0.1 μM $KIF3A_{17}$ in mADP was flushed against varying [Mt] with 500 μM ATP, resulting in sequential release of both bound mADP. *Solid squares*, single exponential fits to experimental data (average of $n = 5–6$ traces/[Mt]). *Open circles*, theoretical predictions based on parameter values taken from the k_{on}^{Mt} experiment in Fig. 4*a* and the half-site experiment in Fig. 3*c*. The match between theory and experiment confirms that the bound mADP are released sequentially upon interaction with the microtubule.

centrations, where ATP binding and stepping is considerably faster than the initial microtubule-binding step, the transient could be fit by a single exponential. A kinetic model of the sequential release process was formulated using rate constants determined from the previous k_{on}^{Mt} and half-site experiments (see "Experimental Procedures"). Results from the analytical solution agreed very well with the experiments (Fig. 4*d*), providing a redundant confirmation of these parameters and supporting the contention that the two mADP are released sequentially following microtubule binding.

mADP Exchange Rates in $KIF3A_{17}$ Are Not Modulated by Intramolecular Strain—To investigate the influence of intramolecular strain on nucleotide binding, we used the non-hydrolyzable ATP analog, AMPPNP, to trap the motors in the two-head-bound state (mimicking *state 7* in Fig. 1) and flushed this complex against varying concentrations of mADP. This experiment, which interrogates rates of mADP binding to the leading head, was used previously to convincingly argue that front head gating plays a role in kinesin-1 processivity (24), and it is the most direct test of the front head gating hypothesis. The first control experiment was to confirm that AMPPNP locks KIF3A in a two-head-bound state. Motors with bound mADP were flushed against microtubules in the presence and absence of AMPPNP (Fig. 5*a*). The amplitude in the presence of AMPPNP was approximately double that of microtubules alone, consistent with microtubule binding triggering release of one mADP and the subsequent binding of AMPPNP triggering stepping and release of the second mADP. Next, a half-site release experiment was carried out similar to the experiment in Fig. 3*e*. A solution of motors, microtubules, and mADP was

flushed against varying concentrations of AMPPNP. As seen previously for kinesin-1 (51, 52), AMPPNP binding resulted in a fluorescence fall, consistent with nucleotide binding causing neck linker docking followed by microtubule binding and mADP release by the tethered head (Fig. 5*b*). The extrapolated maximal mADP release rate was $k_{max}^{AMPPNP/HS} = 5.9 \pm 0.5\ s^{-1}$, which is considerably slower than the equivalent rate of 21 ± 0.7 with ATP (Fig. 3*c*). As explained further under "Discussion," this slow rate supports a model for the hydrolysis cycle in which ATP hydrolysis normally precedes binding of the tethered head to the next binding site (*i.e. state 5* in Fig. 1) but allows for a slow transition from state 4 to state 6 if hydrolysis is blocked (not

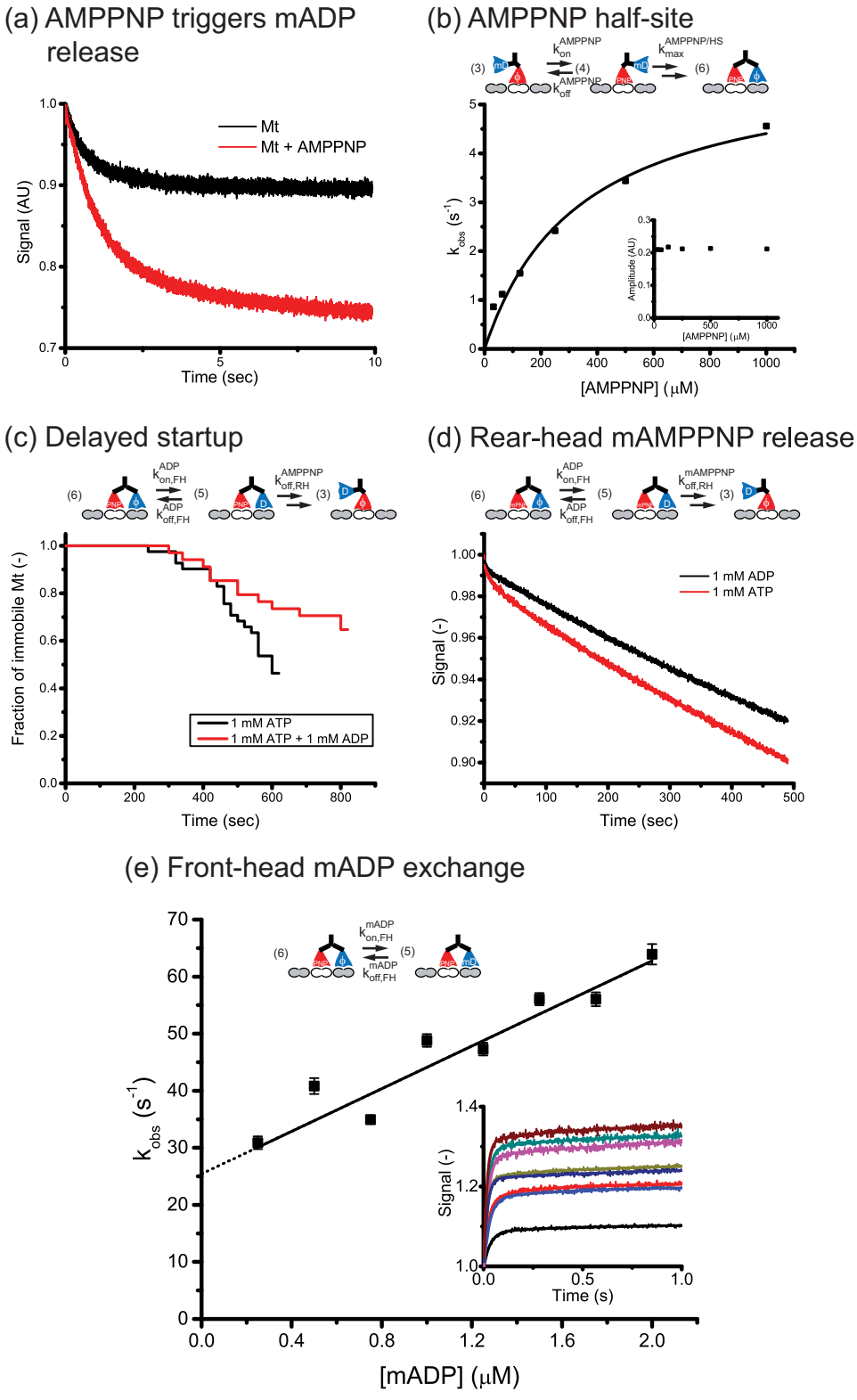

shown in Fig. 1 for clarity). The nucleotide concentration required for half-maximal release ($K_{0.5}^{AMPPNP/HS} = 340 \pm 58$ μM AMPPNP) was considerably higher than the equivalent value in ATP ($K_{0.5}^{ATP/HS} = 5$ μM; Fig. 3*e*), consistent with the motor having a low affinity for AMPPNP. This discrepancy was also observed for kinesin-1 (52), and the low affinity was supported by control experiments that measured the affinity of KIF3A for AMPPNP in solution to be nearly 2 orders of magnitude lower than the affinity for ADP (data not shown). This AMPPNP half-site experiment supports a model in which AMPPNP binding to the bound head results in tethered head binding to the microtubule and releasing its nucleotide, resulting in a two-head-bound state with an empty front head.

After confirming that AMPPNP binding causes KIF3A to transition into a two-head-bound state, we examined the rate at which the motor exits from this AMPPNP-trapped state using a delayed startup experiment as carried out previously for kinesin-1 (53). The delayed startup experiment utilizes the microtubule gliding assay with the following three steps: (*i*) microtubules are introduced in the presence of ATP, resulting in microtubules landing and gliding over the motor-coated surface; (*ii*) AMPPNP is introduced, which results in an arrest of gliding and microtubules binding strongly to the surface; and (*iii*) AMPPNP is washed out, ATP is washed into the flow cell, and the resumption of microtubule gliding is monitored. Results in Fig. 5*c* show that, following the removal of AMPPNP and the addition of ATP, microtubule gliding is delayed for more than 200 s, consistent with motors remaining trapped in the two-head-bound state with AMPPNP in the rear head. This result is consistent with that seen previously with kinesin-1 (53) and demonstrates the robustness of the trapped two-head-bound state. If the front head were to release from the microtubule, then, based on the high $K_{0.5}^{AMPPNP/HS}$ of the AMPPNP half-site experiment in Fig. 5*b*, the AMPPNP would be expected to readily dissociate.

To confirm that AMPPNP remains trapped in this two-head-bound state, we carried out a rear head mAMPPNP exchange assay as follows. Motors and microtubules were incubated with mAMPPNP to drive motors into a two-head-bound state, this complex was flushed against a saturating concentration of ATP or ADP, and the fluorescence fall resulting from mAMPPNP release was monitored (Fig. 5*d*). Both traces showed a slow fluorescence fall, having a time constant longer than 1000 s, consistent with the mAMPPNP remaining stably trapped in the two-head-bound complex. In summary, these control experiments establish that AMPPNP binding causes the motor to enter a stable two-head-bound state with an empty front head, a necessary prerequisite for observing the kinetics of nucleotide exchange in the front head.

To determine the mADP exchange rate in this strained state, motors were incubated with microtubules and AMPPNP, this solution was flushed against varying concentrations of mADP, and the rise in fluorescence resulting from mADP binding was monitored (Fig. 5*e*). Similar to the unstrained exchange experiment shown in Fig. 4*b*, a linear fit to the data yields both the on- and off-rates. From Fig. 5*e*, the mADP off-rate, $k_{off,FH}^{mADP}$, was 25 ± 3 s^{-1}, and the on-rate, $k_{on,FH}^{mADP}$ was 19 ± 3 μM mADP^{-1} s^{-1}. These rates are very similar to the unstrained rates of 27 s^{-1} and 18 μM mADP^{-1} s^{-1}, respectively, from Fig. 4*b*. Hence, these data provide direct evidence that the on- and off-rates of mADP binding to KIF3A are not influenced by intramolecular strain and argue that front head gating does not play a role in kinesin-2 mechanochemistry.

The mATP On-rate Is Also Not Modulated by Interhead Tension in KIF3A—Although mADP exchange rates argue against front head gating in KIF3A, the normal hydrolysis cycle involves binding of ATP and not ADP. Hence, we repeated the exchange experiments using mATP. As seen in Fig. 6*a*, in the unstrained case, k_{on}^{mATP} for $KIF3A_{17}$ was 18 ± 2 μM mATP^{-1} s^{-1}, and the apparent off-rate $k_{off,app}^{mATP}$ was 31 ± 3 s^{-1}. One complexity of this off-rate measurement is that, instead of nucleotide dissociation, mATP can also lead to motor stepping (Fig. 6*a*, *inset*). As described below, simulations were carried out for the entire hydrolysis cycle of KIF3A, and taking the competing pathways into account, the true unstrained mATP off-rate was estimated at 26 s^{-1} (Table 2).

When AMPPNP was used to trap the motor in the two-head-bound state, the mATP exchange rates were $k_{on,FH}^{mATP} = 15 \pm 1$ μM mATP^{-1} s^{-1} and $k_{off,FH}^{mATP} = 36 \pm 2$ s^{-1} (Fig. 6*b*), similar to the equivalent mADP exchange rates (Fig. 5*e*). Thus, the mATP results support the contention that front head gating is not present in KIF3A.

Shortening the Neck Linker Does Not Substantially Alter Nucleotide Exchange Rates—We next asked the question of whether the lack of front head gating in KIF3A results from its longer neck linker compared with kinesin-1. If front head gat-

FIGURE 5. **Front head mADP exchange rates in the two-head-bound state.** *a*, comparison of mADP release amplitudes in the presence and absence of AMPPNP. 0.035 μM dimeric motor with stoichiometric bound mADP were flushed against 2 μM Mt alone (*black*, *top trace*) or 2 μM Mt plus 2 mM AMPPNP (*red*, *bottom trace*). Fluorescence traces were fit with a biexponential, giving a total amplitude of 0.104 in the absence of AMPPNP and 0.269 in the presence of AMPPNP, consistent with a loss of one mADP upon Mt binding and loss of a second mADP upon AMPPNP binding and motor stepping. The amplitude from microtubules alone is less than half due to residual binding of mADP to the motor-bound head (K_D^{mADP} estimated at 1.5 μM from Fig. 4*b*). *b*, half-site nucleotide release triggered by AMPPNP. 0.05 μM motor with 2 μM Mt in mADP were flushed against varying [AMPPNP], and the fluorescence fall resulting from stepping and release of the bound mADP was monitored. From the *fit*, $k_{max}^{AMPPNP/HS} = 5.9 \pm 0.5$ s^{-1} and $K_{0.5}^{AMPPNP/HS} = 340 \pm 58$ μM AMPPNP, $n = 5$–6. *Inset*, amplitude of mADP release. *c*, delayed startup in the Mt gliding assay. Microtubule gliding over a $KIF3A_{17}$-functionalized surface in 1 mM ATP was arrested by the introduction of 1 mM AMPPNP. At $t = 0$, AMPPNP was washed out and replaced with 1 mM ATP with or without 1 mM ADP, and the resumption of movement, quantified as the fraction of immobilized microtubules, was plotted. *d*, nucleotide-stimulated release of mAMPPNP from a KIF3A-Mt-mAMPPNP complex. A solution of 0.1 μM $KIF3A_{17}$, 2 μM Mt, and 33 μM mAMPPNP was preincubated to generate a two-head-bound complex, and this solution was flushed against 1 mM ATP (*black*) or 1 mM ADP (*red*) to release the bound mAMPPNP. The fluorescence fall was fit to a biexponential with a slow rate of 0.000783 ± 0.000012 and 0.000722 ± 0.0000096 s^{-1} for release by ADP and ATP, respectively. The slow rates accounted for 98 and 97% of the amplitude, respectively, with a second process at ~0.2 s^{-1} accounting for the residual amplitude. The slow fluorescence fall is consistent with the trapped AMPPNP in the delayed startup results. *e*, mADP exchange rate in the front head of a two-head-bound motor. A complex of 0.1 μM $KIF3A_{17}$, 2 μM Mt, and 200 μM AMPPNP was flushed against varying concentrations of mADP. A reversible binding model gave $k_{on}^{mADP} = 19 \pm 3$ μM mADP^{-1} s^{-1} and $k_{off,FH}^{mADP} = 25 \pm 3$ s^{-1}, similar to the unstrained exchange rates in Fig. 4*b*. This similarity in rates suggests that when both heads are bound to the microtubule, intramolecular tension does not alter the kinetics of nucleotide binding to the front head. *Inset*, raw fluorescence traces (average of $n = 15$–17 at each [mADP]) and fits. *Error bars*, S.E. of fits.

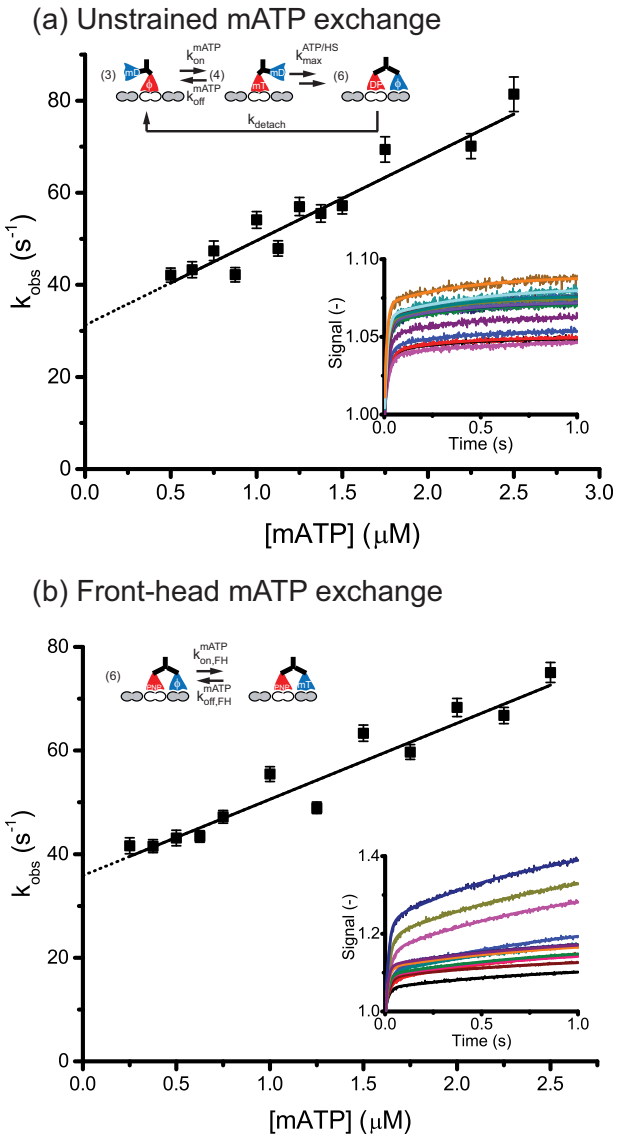

FIGURE 6. **Strained and unstrained mATP exchange rates in KIF3A.** *a*, kinetics of mATP exchange in an unstrained head. A complex of 0.1 μM $KIF3A_{17}$ and 2 μM Mt was flushed against varying concentrations of mATP, and the rise in fluorescence due to mATP binding was monitored. Data were fit by a reversible binding model with $k_{on}^{mATP} = 18 \pm 2$ μM $mATP^{-1}$ s^{-1}. *Inset*, raw traces (average of $n = 13–16$ per [mATP]) with fits. *b*, mATP exchange rate in the front head of a two-head-bound motor. A complex of 0.2 μM $KIF3A_{17}$, 4 μM Mt, and 200 μM AMPPNP was preincubated and flushed against varying concentrations of mATP, similar to Fig. 5*e*. The mATP exchange rates were $k_{on,FH}^{mATP} = 15 \pm 1$ μM $mATP^{-1}$ s^{-1} and $k_{off,FH}^{mATP} = 36 \pm 2$ s^{-1}, similar to those for mADP (Fig. 5*e*). *Inset*, raw traces (average of $n = 13–16$ at each [mATP]) with fits. *Error bars*, S.E. of fits.

ing in kinesin-1 results from rearward strain on the front head, then extending the neck linker that connects the two heads could partially relieve this strain. To test this hypothesis, we repeated the strained and unstrained nucleotide binding experiments using $KIF3A_{14}$, which has a shorter neck linker. If the magnitude of interhead strain is the key determinant of front head gating, then the nucleotide on-rate for $KIF3A_{14}$ should be slower and/or the off-rate should be faster than for $KIF3A_{17}$. As expected, the unstrained mADP exchange rates for $KIF3A_{14}$ ($k_{on}^{mADP} = 15 \pm 1$ μM $mADP^{-1}$ s^{-1}, $k_{off}^{mADP} = 29 \pm 2$ s^{-1}) were similar to those for $KIF3A_{17}$ (Fig. 7*a*). The same control experiments for the AMPPNP-trapped state were then carried out, and the $KIF3A_{14}$ results were shown to be comparable with those for $KIF3A_{17}$ (Fig. 7, *b* and *c*). Finally, the exchange rates for $KIF3A_{14}$ in the two-head-bound state were measured and found to be $k_{on,FH}^{mADP} = 11 \pm 1$ μM $mADP^{-1}$ s^{-1} and $k_{off}^{mADP} = 27 \pm 1$ s^{-1} (Fig. 7*d*), similar to the equivalent rates for $KIF3A_{17}$. These mADP results confirm that the lack of front head gating seen for $KIF3A_{17}$ is not due to its longer neck linker and resultant decrease in interhead tension.

As a final step, we measured the strained and unstrained mATP exchange rates for $KIF3A_{14}$ (Fig. 8, *a* and *b*). From the slopes, the mATP on-rates were 19 ± 1.3 and 11 ± 1 μM $mATP^{-1}$ s^{-1} for the unstrained and strained cases, respectively. Thus, for $KIF3A_{14}$ in the strained state, the apparent mATP on-rate is 2-fold slower. This result suggests that when interhead strain is enhanced by shortening the neck linker, minimal front head gating may be present in the kinesin-2 hydrolysis cycle. However, as expanded upon under "Discussion," this conclusion is tempered by the fact that assessment of mATP binding rates is complicated by the competing reactions of hydrolysis and motor stepping as well as the fact that for mADP there were no substantial differences between the strained and unstrained exchange rates for $KIF3A_{14}$ (Fig. 7, *a* and *b*).

Solving the Entire KIF3A Hydrolysis Cycle—Using all of the measured rate constants and the scheme in Fig. 1, we developed a complete model of the KIF3A hydrolysis cycle for both mATP and unlabeled ATP. The mant-moiety was assumed to not alter the rate of hydrolysis or the microtubule binding and unbinding rate of the motor. Three unspecified parameters, the rate of front head attachment (k_{attach}), the rate of rear head detachment (k_{detach}), and the rate of ATP hydrolysis (k_{hyd}) were estimated from the measured parameters and the overall cycle rate, as described in Table 2. The off-rate of mADP from KIF3A in solution was 15-fold slower than the unlabeled ADP off-rate (Fig. 3*b*), and the ratio of affinities was similar (Fig. 3*a*). Thus, the on-rates for unlabeled ADP and ATP binding in Table 2 were taken directly from the measured mant-nucleotide on-rates, and unlabeled ADP and ATP off-rates were estimated as 15-fold slower than the corresponding mADP and mATP off-rates.

The first test of the model was to determine whether it could recapitulate single-molecule motility behavior of KIF3A. A Monte Carlo simulation (described under "Experimental Procedures"; code available as supplemental material) was carried out using the framework of Fig. 1 and the parameters from Table 2. As seen in Fig. 9, *a–c*, run length and motor velocity matched previous measurements (28). Next, simulations were carried out to confirm the self-consistency of the model with the experimental results. To do this, the sequence of transitions interrogated by each stopped-flow experiment was modeled, and the rates were compared with experimental results (described under "Experimental Procedures"; code available as supplemental material). The model was able to recapitulate the entire experimental data set with reasonable accuracy (Fig. 9, *d–k*). This self-consistency provides further support for the framework of Fig. 1 and the parameter values in Table 2.

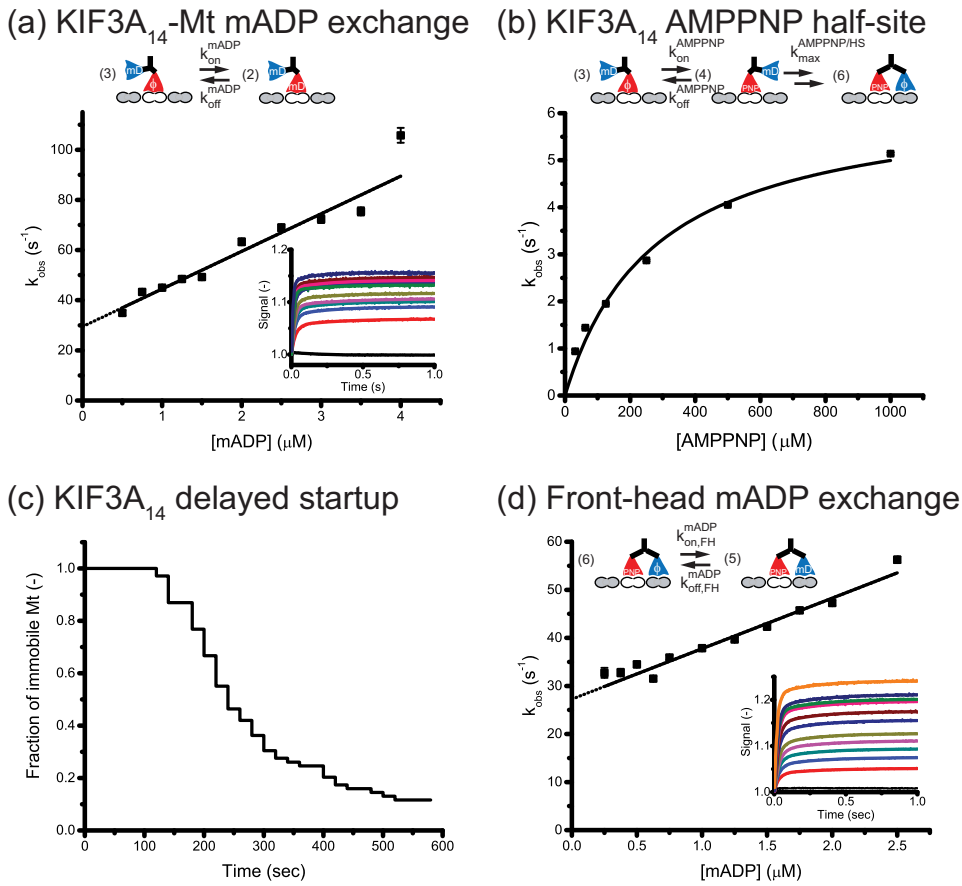

FIGURE 7. **Effect of shortening neck linker on strained and unstrained mADP exchange rates.** Experiments were repeated for KIF3A$_{14}$, which has its neck linker shortened to match that of kinesin-1. *a*, KIF3A$_{14}$-Mt (0.1 μM motor with 2 μM Mt) complex was flushed against varying concentrations of mADP, and the fluorescence rise was fit to an exponential with rate constant k_{obs}. Fitting a line to k_{obs} resulted in $k_{on}^{mADP} = 15 \pm 1$ μM mADP^{-1} s^{-1} and $k_{off}^{mADP} = 29 \pm 2$ s^{-1}, which are similar to corresponding rates for KIF3A$_{17}$ in Fig. 4*b*. *Inset*, raw traces at varying [mADP] (average of n = 15–17/[mADP]) and fits. *b*, AMPPNP half-site experiment for KIF3A$_{14}$. 0.05 μM motor, 2 μM Mt with stoichiometric mADP was flushed against varying [AMPPNP]. Results of fit were $k_{max}^{AMPPNP/HS} = 6.4 \pm 0.4$ s^{-1} and $K_{0.5}^{AMPPNP/HS} = 278 \pm 44$ μM AMPPNP (n = 5–6). *c*, delayed startup in the KIF3A$_{14}$ gliding assay indicates similar trapping of AMPPNP as in KIF3A$_{17}$ (n = 69 Mt). *d*, front head mADP exchange. A complex consisting of 0.2 μM KIF3A$_{14}$, 2 μM Mt, and 200 μM AMPPNP was preincubated and flushed against varying [mADP]. Single exponentials were fit to the fluorescence rise, and the resulting exchange rate was fit by a line, resulting in $k_{on,FH}^{mADP} = 11 \pm 1$ μM mADP^{-1} s^{-1} and $k_{off}^{mADP} = 27 \pm 1$ s^{-1}. *Inset*, raw traces (average of n = 15–17 at each [mADP]) with fits. *Error bars*, S.E. of fits.

As a final test of the model, we simulated microtubule gliding assays at varying nucleotide concentrations. In Table 2, the binding kinetics of unlabeled ADP and ATP were extrapolated from the mant-nucleotide values. Hence, simulating motor stepping at varying ATP and ADP concentrations provides an independent test of the accuracy of these rate constants. In 0.5 mM ATP, the motor stepping rate as determined from the gliding speed was 47 ± 5 s^{-1}, matching previous results from single-molecule experiments (18), and when 0.5 and 2 mM concentrations of ADP were added, the stepping rates fell to 27 ± 3 and 15 ± 2 s^{-1}, respectively (Fig. 9*l*). Results from model simulations using these same nucleotide conditions were in good agreement with experiments, further supporting the validity of the model.

DISCUSSION

The goal of this study was to characterize the entire chemomechanical cycle of the kinesin-2 motor KIF3A and thereby determine the gating mechanisms that determine its processivity. The kinesin-2 KIF3A/B differs from the canonical kinesin-1 in a number of ways. Structurally, the wild-type motor is a heterodimer with a 17-residue neck linker compared with the 14-residue kinesin-1 neck linker domain (28, 54, 55). Functionally, the wild-type motor is less processive than kinesin-1, and it dissociates more readily under load (18, 28, 29, 56). From the biochemical perspective, however, little is known regarding differences between hydrolysis cycles of kinesin-2 and kinesin-1 that may explain their functional differences.

The first striking finding in this work was that, although $K_{0.5}^{Mt}$ from the ATPase and K_D^{Mt} from pelleting assays in ATP were similar for kinesin-1 and KIF3A, KIF3A had a relatively high microtubule affinity in ADP and had a Mt dissociation rate in ADP (2.1 s^{-1}) that is 20-fold slower than the stepping rate. It was shown previously that the kinesin-3, KIF1A/Unc104, has a high microtubule affinity in the ADP state, which enables monomers to move processively under certain conditions (57) and is thought to contribute to the reported "superprocessivity" of dimers (58). This enhanced microtubule affinity was shown to result from the ionic interaction between the positively charged loop 12 (K-loop) of the motor and the negatively charged C terminus (E-hook) of β-tubulin (57, 59). Based on sequence alignments in loop 12 (Fig. 10), kinesin-2 has more positive charge in the K-loop (net charge of +2) than kinesin-1 (+1) but less than kinesin-3 (+6). For comparison, the K_D^{Mt} of

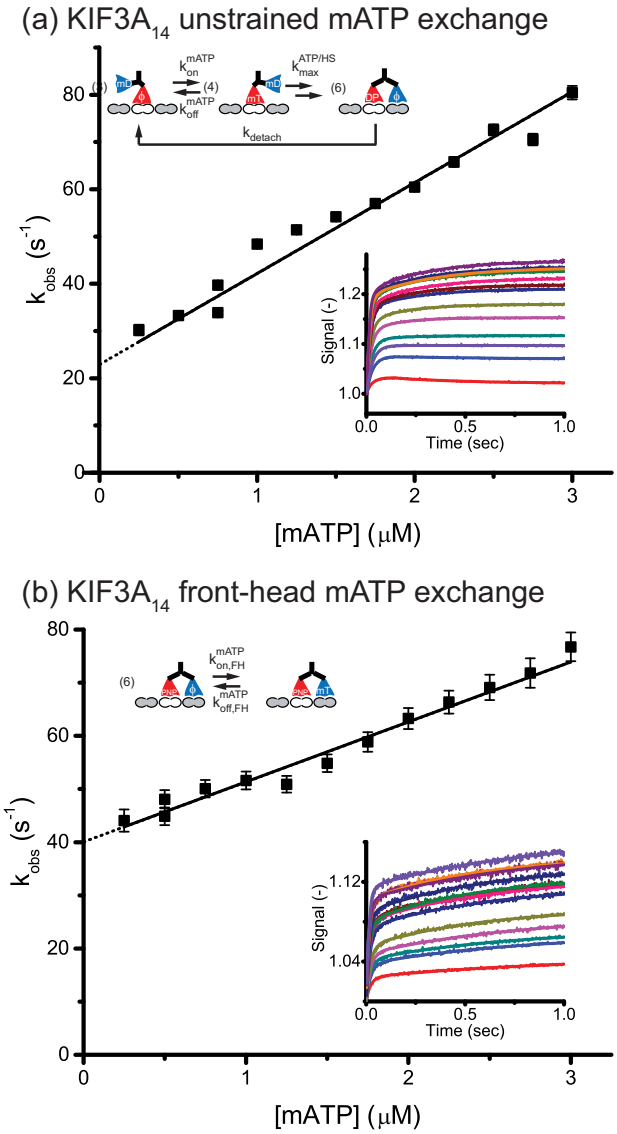

FIGURE 8. **mATP exchange kinetics in KIF3A$_{14}$.** *a*, kinetics of mATP exchange in unstrained head of KIF3A$_{14}$. A complex of 0.2 μM KIF3A$_{14}$ and 2 μM Mt was flushed against varying concentrations of mATP, and the rise in fluorescence due to mATP binding was monitored. Data were fit by a reversible binding model with $k_{on}^{mATP} = 19 \pm 1.3$ μM mATP^{-1} s^{-1}. *Inset*, raw traces (average of $n = 13$–17/[mATP]) with fits. *b*, mATP exchange rate in the front head of two-head-bound KIF3A$_{14}$ motor. A complex of 0.2 μM KIF3A$_{14}$, 2 μM Mt, and 200 μM AMPPNP was preincubated and flushed against varying concentrations of mATP, similar to Fig. 6*b*. The mATP exchange rates from the linear fit were $k_{on,FH}^{mATP} = 11 \pm 1$ μM mATP^{-1} s^{-1} and $k_{off,FH}^{mATP} = 40 \pm 1$ s^{-1}. *Inset*, raw traces (average of $n = 13$–17 at each [mATP]) with fits. *Error bars*, S.E. of fits.

monomeric KIF1A in ADP was ~5 nM (in 50 mM imidazole plus 50 mM potassium acetate buffer (59)), nearly 100-fold tighter than the 0.45 μM K_D^{Mt} for KIF3A and 2000-fold tighter than the 11 μM K_D^{Mt} for kinesin-1 measured here. The fact that each added positive charge in loop 12 was shown previously to contribute 0.25 k_BT of binding energy (59), whereas the kinesin-1/kinesin-2 difference corresponds to 3.2 k_BT for one added charge and the kinesin-2/kinesin-3 difference corresponds to 4.5 k_BT for four added charges, suggests that loop 12 is not the sole determinant of the enhanced microtubule affinity of kinesin-2 in ADP. Notably, the neck-coil region, which has been shown to modulate processivity in some cases through electrostatic interactions with the microtubule (60), is identical for the kinesin-1 and kinesin-2 constructs used here. Hence, the binding affinity of kinesin-2 in the weak binding state is intermediate between that of kinesin-1 and kinesin-3. If the simplification can be made that kinesin-3 maintains processivity due to the high microtubule affinity of its weak binding state and kinesin-1 maintains processivity through tight coordination between the hydrolysis cycles of the two heads, then kinesin-2 falls between these two mechanisms.

Because kinesin-2 has a higher microtubule affinity in its weak binding state, it might be predicted to be more processive than kinesin-1. However, kinesin-2 was previously shown to be 4-fold less processive than kinesin-1 (27). One resolution to this paradox is that kinesin-2 spends a much larger fraction of its hydrolysis cycle in a weak binding state, providing a greater chance for dissociation. Previous work on kinesin-1 suggested that the motor spends <5% of its cycle in a one-head-bound weak binding state in saturating ATP (61). In contrast, the similarity in microtubule affinities in ATP and ADP (Fig. 2, *b*–*d*; pelleting assays) suggests that KIF3A spends a large fraction of its ATPase cycle in the weak binding state, although the data do not provide rigorous constraints. In the KIF3A hydrolysis cycle formulated in Fig. 1 and Table 2, the motor spends 43% of its hydrolysis cycle in the weak binding state (state 5), but because of uncertainties in estimating k_{attach}, this value is also not tightly constrained by the data. Further support comes from the finding that KIF3A maintains processivity when mATP is used as the substrate (Fig. 3*c*, *inset*). If the motor only spent a small fraction of its cycle in the low affinity state (state 5) and dissociation from this state determined processivity, then making this the longest lived state in the hydrolysis cycle by slowing product release should strongly reduce processivity. This is not the case; despite mADP release being the rate-limiting step (15-fold slower than for unlabeled ADP), the run length is not substantially reduced in mATP. Thus, the best resolution of the paradoxical affinity and processivity measurements is to conclude that kinesin-2 spends a larger fraction of its hydrolysis cycle in a weak binding state, but that state has a higher microtubule affinity than the corresponding state for kinesin-1.

The second striking finding of this study was that interhead strain in KIF3A had no effect on nucleotide binding kinetics. This result, summarized in Table 1, contrasts with the widely accepted model for front head gating in kinesin-1 (22, 24, 25) and suggests that front head gating plays no role in KIF3A processivity. The lack of effect of strain on mADP exchange was shown in two ways. The one-head-bound mADP exchange experiment in Fig. 4*b* measured the unstrained rate, and both the half-site experiment in Fig. 3*e* and the front head mADP exchange experiment in Fig. 5*e* measured the strained rate and found similar kinetics. When the neck linker domain was shortened from 17 to 14 residues in an effort to enhance interhead strain in the two-head-bound state, mADP exchange kinetics were similarly unchanged. The only evidence that interhead strain may inhibit nucleotide binding was for mATP binding to KIF3A$_{14}$, where the unstrained on-rate of 19 μM mATP^{-1} s^{-1} was nearly 2-fold faster than the strained on-rate of 11 μM mATP^{-1}s^{-1} (Table 1). However, because measurement of k_{on}^{mATP} is complicated by the competing ATP hydrolysis and stepping pathways, precise determination is somewhat model-

(a) Run length

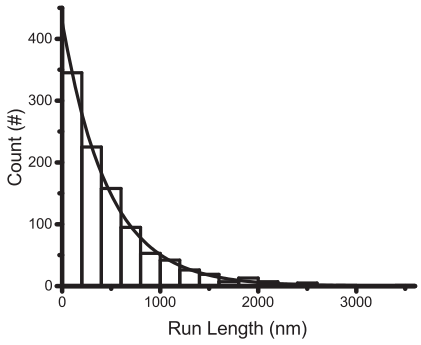

(b) Velocity

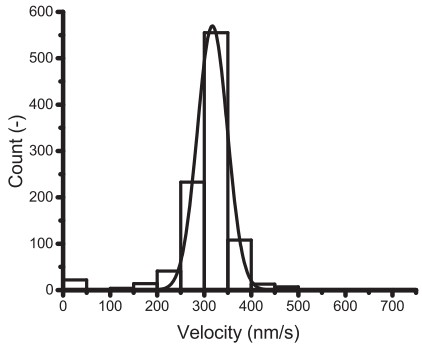

(c) Step duration

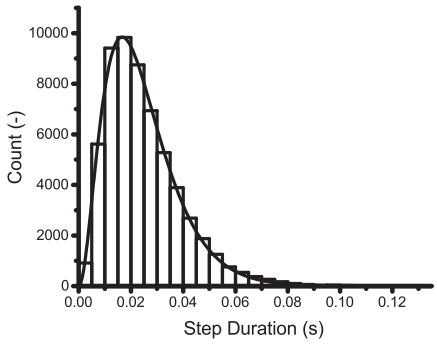

(d) Unstrained mADP exchange

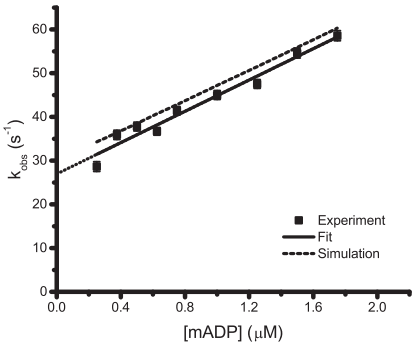

(e) k_{on}^{Mt} experiment

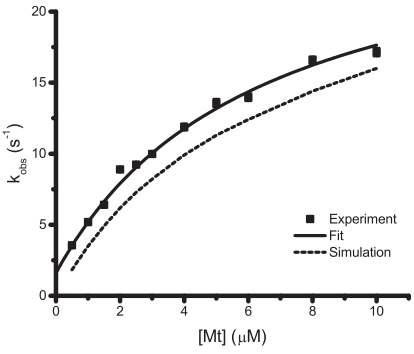

(f) ATP half-site assay

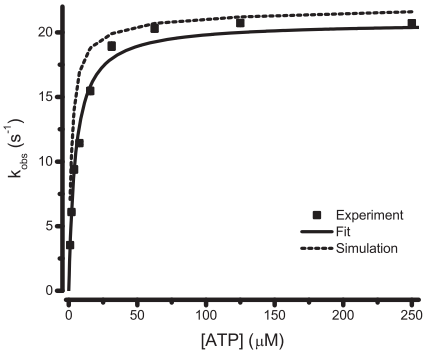

(g) Sequential release assay

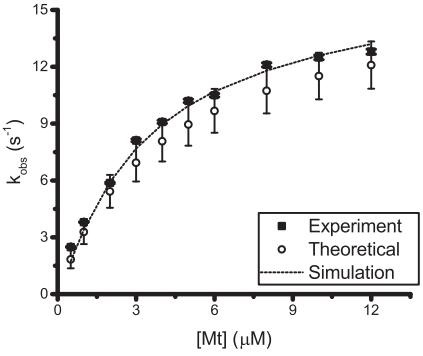

(h) Front-head mADP exchange

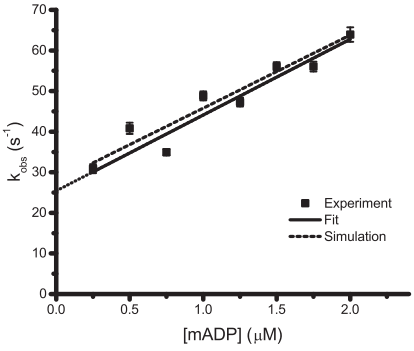

(i) Front-head mATP exchange

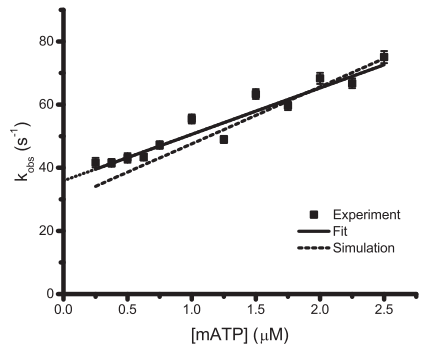

(j) Unstrained mATP exchange

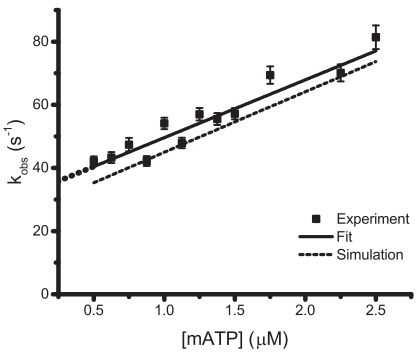

(k) Gliding with mATP

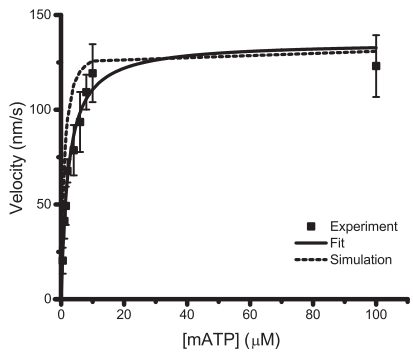

(l) Gliding inhibition by ADP

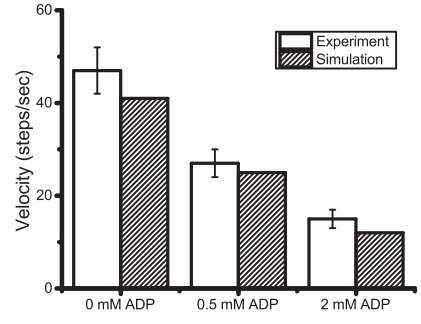

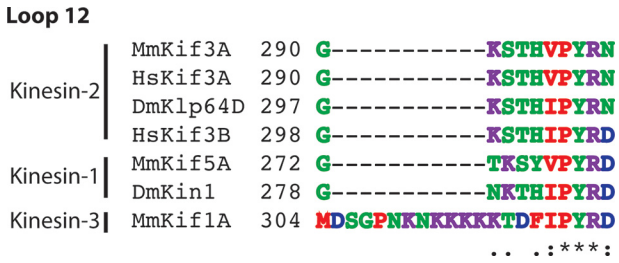

FIGURE 10. **Comparison of loop 12 sequences.** Multiple-sequence alignment was carried out using ClustalW2. In loop 12, MmKIF1A has one less negative charge than DmKHC, but neither has the K-loop insert of KIF1A.

TABLE 1
Mant-nucleotide exchange rates under different conditions

State	mADP		mATP	
	1-HB[a]	2-HB[b]	1-HB[a]	2-HB[b]
$KIF3A_{17}$				
k_{on} (μM^{-1} s^{-1})	18	19	18	15
k_{off} (s^{-1})	27	25	ND[c]	36
$KIF3A_{14}$				
k_{on} (μM^{-1} s^{-1})	15	11	19	11
k_{off} (s^{-1})	29	27	ND	40

[a] 1-HB is the one-head-bound state, obtained by mixing motors and microtubules.
[b] 2-HB is the two-head-bound state, obtained by mixing motors, microtubules, and AMPPNP.
[c] ND, not determined.

dependent, and a much smaller strain dependence was seen for k_{on}^{mADP}. Furthermore, at standard conditions of 1 mM ATP, this change in k_{on}^{mATP} corresponds to an increase in the ATP waiting state (*state 7* in Fig. 1) from 53 to 91 μs, both of which are very fast relative to other rates in the hydrolysis cycle.

Besides the mADP binding evidence in support of front head gating in kinesin-1 (24), strain-dependent nucleotide binding in kinesin-1 is also supported by forced unbinding experiments at varying [ADP] (26), the slow startup observed following AMPPNP or BeFx treatment (22, 53), phosphate release kinetics of a mutant (23), and the finding from optical tweezers experiments that the K_m^{ATP} for motor velocity is load-dependent (62, 63). Interestingly, similar optical tweezers experiments on full-length KIF3A/B heterodimer found K_m^{ATP} at 0- and 4-piconewton loads to be similar, providing independent evidence that nucleotide binding is less load-dependent in kinesin-2 than in kinesin-1 (29).

Using the rate constants given in Table 2 and the model structure shown in Fig. 1, we formulated a complete model for the KIF3A chemomechanical cycle and used it both to test the internal consistency of our kinetics data and to make predictions. The model contains three rate constants that are very difficult to directly measure and thus were constrained based on measured rates. First, the attachment rate of the tethered head following ATP binding and hydrolysis (k_{attach} from state 5) was chosen as 117 s^{-1} based on the measured k_{unbind} of 2.1 s^{-1} and the previous finding that the motor takes 56 steps before detaching (28). Second, the trailing head detachment rate (k_{detach} from state 7) was chosen as 89 s^{-1} based on the difference between the half-site mADP release rate (which encompasses the entire cycle except k_{detach}) and the overall cycle rate from the gliding assay. Third, the ATP hydrolysis rate was chosen to be fast relative to other steps at 478 s^{-1}, as shown in Table 2, but this value was not tightly constrained (range of 47–967 s^{-1}). Importantly, using these three inferred parameters and all of the measured rate constants, the model recapitulated the overall stepping rate of 40 s^{-1}, and stepping data from stochastic simulations had a randomness of 0.34 due to the two rate-limiting steps of front head attachment and rear head detachment (Fig. 9, *a–c*), similar to that measured for full-length KIF3A/B in optical tweezers experiments (29). Furthermore, we were able to simulate all of the kinetics experiments and show that the model agrees with the experimental data (Fig. 9, *d–k*).

The hydrolysis model also enables a quantitative explanation of the roles of front and rear head gating in determining motor processivity. Based on the measured nucleotide binding rates and inferred rear head detachment rate, during the normal KIF3A stepping cycle, ATP binds to the front head before the trailing head detaches (*i.e.* state 8 is preferred over state 3). Importantly, the key to processivity is the race (from state 5) between detachment of the bound head and attachment of the tethered head. Milic *et al.* (42) recently showed that tethered head binding occurs subsequent to ATP hydrolysis in kinesin-1, which means that whatever the states preceding it, the motor must pass through the susceptible one-head-bound state (state 5). Thus, the key quantitative feature of rear head gating is not the rate at which the trailing head detaches in the strained state (k_{attach}) but rather the rate of unbinding from the vulnerable one-head-bound state (k_{unbind}). A corollary is that if unbinding from the weak binding state is slow, then front head gating does not enhance processivity.

One unresolved question is why the AMPPNP-trapped two-head-bound state is so long lived. This minutes-long state was observed previously in gliding assays (53) and in optical tweezers experiments that showed that resumption of walking resulted from the motor back-stepping, presumably to release the bound inhibitor, and then resuming forward stepping (22). The fact that fresh ATP is required for the motor to exit the state shows that AMPPNP is trapped, and mAMPPNP exchange experiments (Fig. 5*d*) support this. However, the pathway that untraps the motor is not clear. One hypothesis is that due to front head gating, ATP binding to the front head is blocked, and slow ATP binding is the trigger, but this is ruled out for KIF3A by the strained ATP binding measurements (Fig.

FIGURE 9. **Confirmation of the KIF3A hydrolysis cycle model.** Using the hydrolysis model shown in Fig. 1 and the rate constants in Table 2, motor stepping simulations were run as described previously (35). *a*, distribution of run lengths from 1000 simulated runs at 1 mM ATP. A monoexponential fit to the distribution yielded a mean run length of 470 ± 9 nm, matching previous single-molecule results (19). *b*, distribution of single-molecule velocities, with mean ± S.D. (*error bars*) of 317 ± 32 nm/s from a Gaussian fit. *c*, distribution of step durations. Data were fit to a γ distribution with a shape parameter of 3.14 ± 0.04, and the randomness parameter was calculated to be 0.34 (15, 34). *d–k*, simulations of all stopped-flow kinetics experiments for $KIF3A_{17}$, showing self-consistency between experiments and simulations. *Circles*, experimental results. *Solid curve*, least-squares fit to experimental data. *Dashed curve*, simulation results. *l*, gliding assays in 0.5 mM ATP and varying ADP concentrations (mean ± S.D. for n = 41–42 microtubules at each [ADP]; gliding speeds are shown in steps/s by dividing by 8 nm/step), showing agreement of experimental results with predictions from simulations. MATLAB code used for all simulations is included as supplemental material.

TABLE 2
Rate constants for the kinesin-2 chemomechanical cycle

Transition	Rate constant	Description	Source	Experiment	Simulation	Units
1-2	k_{bind}	Bound head Mt on-rate	Derived[a]	4.6 ± 0.9	4.6	$\mu M^{-1}\ s^{-1}$
2-1, 5-1	k_{unbind}	Bound head Mt off-rate	Fig. 2*f*	2.1 ± 0.2	2.1	s^{-1}
2-3	k_{off}^{ADP}	Bound head ADP off-rate	Derived[b]		390	s^{-1}
	k_{off}^{mADP}	Bound head mADP off-rate	Fig. 4*b*	27 ± 1.3	26	s^{-1}
3-2	k_{on}^{ADP}	Bound head ADP on-rate	Derived[b]		18	$\mu M^{-1}\ s^{-1}$
	k_{on}^{mADP}	Bound head mADP on-rate	Fig. 4*b*	18 ± 1.3	18	$\mu M^{-1}\ s^{-1}$
3-4	k_{on}^{ATP}	Bound head ATP on-rate	Derived[b]		18	$\mu M^{-1}\ s^{-1}$
	k_{on}^{mATP}	Bound head mATP on-rate	Fig. 6*a*	18 ± 2	18	$\mu M^{-1}\ s^{-1}$
4-3	k_{off}^{ATP}	Bound head ATP off-rate	Derived[b]		390	s^{-1}
	k_{off}^{mATP}	Bound head mATP off-rate		ND[c]	26	s^{-1}
4-5	k_{hyd}	Hydrolysis rate	Derived[d]	(47, 967)[e]	478	s^{-1}
5-6	k_{attach}	Front head attachment rate	Derived[f]	117 ± 14	117	s^{-1}
6-7	$k_{off,FH}^{ADP}$	Front head ADP off-rate	Derived[b]		390	s^{-1}
	$k_{off,FH}^{mADP}$	Front head mADP off-rate	Fig. 5*d*	25 ± 3	26	s^{-1}
7-6	$k_{on,FH}^{ADP}$	Front head ADP on-rate	Derived[b]		18	$\mu M^{-1}\ s^{-1}$
	$k_{on,FH}^{mADP}$	Front head mADP on-rate	Fig. 5*d*	19 ± 3	18	$\mu M^{-1}\ s^{-1}$
7-3, 8-4	k_{detach}	Rear head detachment rate	Derived[g]	89 ± 25	89	s^{-1}
7-8	$k_{on,FH}^{ATP}$	Front head ATP on-rate	Derived[b]		18	$\mu M^{-1}\ s^{-1}$
	$k_{on,FH}^{mATP}$	Front head mATP on-rate	Fig. 6*b*	15 ± 1	18	$\mu M^{-1}\ s^{-1}$
8-7	$k_{off,FH}^{ATP}$	Front head ATP off-rate	Derived[b]		390	s^{-1}
	$k_{off,FH}^{mATP}$	Front head mATP off-rate	Fig. 6*b*	36 ± 2	26	s^{-1}

[a] In Fig. 4*a*, $K_{0.5}^{Mt} = k_{unbind} + k_{off}^{mADP}/k_{bind}$.
[b] Based on the 15-fold difference in KIF3A affinity for mant- *versus* unlabeled nucleotides in solution (Fig. 3, *a* and *b*).
[c] ND, not determined.
[d] In Fig. 3*e*, $1/k_{max}^{ATP/HS} = 1/k_{off,FH}^{mADP} + 1/k_{attach} + 1/k_{hyd}$.
[e] 95% confidence interval with truncated Gaussian model. Lower bound: stepping rate; upper bound: one-tailed, $\alpha = 5\%$.
[f] Processivity (55.6 ± 3.7 steps (28)) = k_{attach}/k_{unbind}.
[g] In Fig. 3*c*, $1/k_{step}^{mATP} = 1/k_{max}^{ATP/HS} + 1/k_{detach}$.

6*b*). A second hypothesis is that ATP can bind but hydrolysis is blocked, but this is ruled out by the fact that adding ADP does not accelerate the startup (Fig. 5, *c* and *d*). The hypothesis that best accounts for the data is that detachment from the microtubule is highly directionally dependent and that even when the front head is in the ADP-P_i or ADP state, its detachment rate is very slow. This hypothesis can be reconciled with forced unbinding measurements on kinesin-1 and kinesin-2 that show only a moderate directional dependence by the fact that the forces imposed by the optical trap include a significant component normal to the microtubule that accelerates detachment, arguing that the true rearward direction experienced by the head in the two-head-bound state is not experimentally accessible (26, 29).

The present work brings into question some of the conclusions from a recent biochemical study by Albracht *et al.* (64) that used similar methods to investigate the hydrolysis cycle of KIF3A/B heterodimers. Both studies used mouse KIF3, and we showed previously that the motility characteristics of heterodimeric KIF3A/B and homodimeric KIF3A/A are similar under unloaded conditions (28). Hence, there is no evidence that discrepancies between the two studies result from differences in the motor constructs employed. As argued below, we contend that our results are in fact consistent with the experimental data of Albracht *et al.* (64), but we differ significantly on the interpretation of the results.

The first conclusion from the Albracht *et al.* study (64) was that ADP release at 12 s^{-1} is the rate-limiting step in the KIF3A/B hydrolysis cycle. This conclusion came from a sequential release experiment (mADP-loaded motors are flushed against microtubules in the presence of saturating ATP, leading to a fall in fluorescence) that was very similar to our sequential release experiments in Fig. 4*d* (which also yielded a rate of 12 s^{-1}). Albrecht *et al.* (64) interpreted this rate as the ADP off-rate from a single head. In contrast, we interpret this process as sequential nucleotide release involving microtubule binding and mADP release from the first head (measured at 26 s^{-1} in the k_{on}^{Mt} experiment in Fig. 4*a*) followed by rapid ATP binding and release of the second mADP (measured at 21 s^{-1} by the half-site experiment in Fig. 3*e*). In Fig. 4*d*, we used a kinetic model to show that sequential release with these measured rates leads to the 12 s^{-1} measured experimentally. More importantly, we show in Fig. 3 that the affinity of KIF3 motors for mADP is 15-fold higher than the affinity for unlabeled nucleotide. Hence, we disagree that for the normal ATP hydrolysis cycle, ADP release is rate-limiting, and rather than the 12 s^{-1} from Albracht *et al.* (64), we model k_{off}^{ADP} at 390 s^{-1} (Table 2) based on our work. This high affinity for mant-nucleotides may also partly explain the high apparent ATP affinity ($K_{d,ATP} = 6.1$ μM from mATP binding) that Albracht *et al.* (64) were unable to reconcile with their measured ATP dependence of ATPase and motor detachment (118 and 133 μM, respectively, using unlabeled ATP).

The second discrepancy with the previous work was that Albracht *et al.* (64) contend that ATP hydrolysis is partially rate-limiting at 33 s^{-1} for KIF3A/B, which contrasts with our modeled hydrolysis at 478 s^{-1} (Table 2). From acid quench experiments involving rapid mixing of ATP with preformed KIF3A/B-Mt complex, Albracht *et al.* (64) measured a burst of ATP hydrolysis at 33 s^{-1}, with the key detail that the amplitude of the burst was 3 ATP/active site (or 6 ATP/dimeric motor). Were the burst amplitude less than or equal to 1 ATP/motor dimer, the data would be consistent with a burst of hydrolysis at 33 s^{-1}, but the burst of 6 ATP/dimer suggests that the experiment is actually measuring multiple steps by the motor and is, at best, only a lower limit for the ATP hydrolysis rate. Our

modeling constrains the ATP hydrolysis rate only weakly (between 47 and 967 s^{-1}; Table 2), but based on our interpretation, this is not inconsistent with the results of Albracht *et al.* (64).

The third discrepancy between the studies concerns the rate of trailing head detachment during motor stepping, which Albracht *et al.* (64) estimate to be 22.3 s^{-1} based on the fall in light scattering resulting from rapidly adding ATP to preformed KIF3A/B-Mt complexes. If the light scattering signal is to be considered a measure of the trailing head detachment rate, then the motor must bind and hydrolyze one ATP molecule and then dissociate without taking a step (because even taking one step would require detachment of both heads for the motor to dissociate). Albracht *et al.* (64) added 100 mM KCl to the buffer to minimize the number of steps before dissociation, but pulse-chase and acid quench experiments under similar conditions showed bursts of 3 ATP/active site (6 ATP/dimeric motor). Thus, a more conservative interpretation of the data is that the rate measured by light scattering provides only a lower limit for trailing head detachment, meaning that it is fully consistent with our estimate for k_{detach} of 89 ± 25 s^{-1} (Table 2).

The final discrepancy with the Albracht *et al.* work concerns the sequence of steps in the hydrolysis cycle. Albracht *et al.* (64) assume that during motor stepping, ATP binding to the bound head leads to stepping followed by ADP release by tethered head, and only then is ATP hydrolyzed by the first head. More precisely, following *state 4* in our Fig. 1 (corresponding to state E3 from Albracht *et al.* (64)), states 5 and 6 are replaced by a two-head-bound state (E4) with no nucleotide in the leading head and ATP in the trailing head, which then resolves to our state 7 (E5). The first problem is that, whereas our framework provides a pathway for motor detachment, the Albracht cycle does not. Second, our framework is supported by recent work by Milic *et al.* (42) that showed that slowing ATP hydrolysis (by using ATPγS) does not enhance processivity, arguing that ATP hydrolysis in the bound head precedes binding and ADP release by the tethered head. Third, although AMPPNP does trigger mADP release by the second head, we found the maximal rate to be only 5.9 s^{-1} (Fig. 5*b*), compared with >47 s^{-1} by the pathway in Fig. 1. Thus, although a bifurcation of the cycle following state 4 cannot be ruled out, at a minimum, stepping before hydrolysis is strongly disfavored kinetically. In summary, although our results are consistent with the experimental data of Albracht *et al.* (64), our interpretations of the results differ markedly.

The present work provides a biochemical framework in which to interpret previous kinesin-2 observations and provides insight into the role of kinesin-2 in cells. It was shown previously that during processive stepping, kinesin-2 readily detaches under load (29, 56, 65). This behavior can be explained by our finding here that the motor spends a significant fraction of its hydrolysis cycle in a weakly bound state that would be expected to detach under load. Kinesin-2 was found to step around obstacles more efficiently than kinesin-1, and beads coated with many kinesin-2 motors were observed to take spiral paths along microtubules, both of which could also be attributed to the motor residing in a weak binding state that can diffuse on the microtubule lattice (66, 67). One question that this work does not answer is why shortening the kinesin-2 neck linker from 17 to 14 residues enhances motor processivity (18). Based on the model for the KIF3A hydrolysis cycle developed here, not only is an effect on front head gating (nucleotide binding) ruled out, but increasing the trailing-head detachment rate by shortening the neck linker is also not predicted to enhance processivity. This question will be best addressed in future experiments by directly measuring the attachment and detachment rate constants in the hydrolysis cycle and determining their dependence on neck linker length.

In terms of its transport function in cells, the fact that kinesin-2 spends a large fraction of its cycle in a microtubule-associated weak binding state means that opposing forces generated by dynein bound to the same cargo will tend to overwhelm kinesin-2. However, the motor is also predicted to maintain its association with the microtubule when it is being pulled in the opposite direction, which may enhance directional switching following the termination of the dynein run. These results highlight the specialization of different kinesin transport motors and provide constraints for understanding bidirectional transport by combinations of different kinesins and opposed teams of kinesins and dyneins.

Acknowledgments—We gratefully acknowledge Nathan Deffenbaugh and Yalei Chen for assistance in preliminary ensemble kinetics simulations and hydrolysis cycle modeling. We thank David Hackney for thoughtful insights on the manuscript and Mark Signs of the Penn State Huck Institutes for Life Sciences Fermentation Facility for assistance in protein expression.

REFERENCES

1. Haraguchi, K., Hayashi, T., Jimbo, T., Yamamoto, T., and Akiyama, T. (2006) Role of the kinesin-2 family protein, KIF3, during mitosis. *J. Biol. Chem.* **281,** 4094–4099
2. Yamazaki, H., Nakata, T., Okada, Y., and Hirokawa, N. (1996) Cloning and characterization of KAP3: a novel kinesin superfamily-associated protein of KIF3A/3B. *Proc. Natl. Acad. Sci. U.S.A.* **93,** 8443–8448
3. Cole, D. G. (1999) Kinesin-II, the heteromeric kinesin. *Cell. Mol. Life Sci.* **56,** 217–226
4. Hirokawa, N., and Noda, Y. (2008) Intracellular transport and kinesin superfamily proteins, KIFs: structure, function, and dynamics. *Physiol. Rev.* **88,** 1089–1118
5. Lin, F., Hiesberger, T., Cordes, K., Sinclair, A. M., Goldstein, L. S. B., Somlo, S., and Igarashi, P. (2003) Kidney-specific inactivation of the KIF3A subunit of kinesin-II inhibits renal ciliogenesis and produces polycystic kidney disease. *Proc. Natl. Acad. Sci.* **100,** 5286–5291
6. Marszalek, J. R., Liu, X., Roberts, E. A., Chui, D., Marth, J. D., Williams, D. S., and Goldstein, L. S. (2000) Genetic evidence for selective transport of opsin and arrestin by kinesin-II in mammalian photoreceptors. *Cell* **102,** 175–187
7. Hancock, W. O. (2014) Bidirectional cargo transport: moving beyond tug of war. *Nat. Rev. Mol. Cell Biol.* **15,** 615–628
8. Hendricks, A. G., Twelvetrees, A. E., and Holzbaur, E. L. F. (2012) Intracellular transport: new tools provide insights into multi-motor transport. *Curr. Biol.* **22,** R1053–R1055
9. Hendricks, A. G., Perlson, E., Ross, J. L., Schroeder, H. W., 3rd, Tokito, M., and Holzbaur, E. L. F. (2010) Motor coordination via a tug-of-war mechanism drives bidirectional vesicle transport. *Curr. Biol.* **20,** 697–702
10. Howard, J. (1995) The mechanics of force generation by kinesin. *Biophys. J.* **68,** 245S–253S; 253S–255S
11. Kaseda, K., Higuchi, H., and Hirose, K. (2003) Alternate fast and slow stepping of a heterodimeric kinesin molecule. *Nat. Cell Biol.* **5,** 1079–1082

12. Hackney, D. D. (1994) Evidence for alternating head catalysis by kinesin during microtubule-stimulated ATP hydrolysis. *Proc. Natl. Acad. Sci. U.S.A.* **91,** 6865–6869
13. Yildiz, A., Tomishige, M., Vale, R. D., and Selvin, P. R. (2004) Kinesin walks hand-over-hand. *Science* **303,** 676–678
14. Hackney, D. D. (1995) Highly processive microtubule-stimulated ATP hydrolysis by dimeric kinesin head domains. *Nature* **377,** 448–450
15. Svoboda, K., and Block, S. M. (1994) Force and velocity measured for single kinesin molecules. *Cell* **77,** 773–784
16. Meyhöfer, E., and Howard, J. (1995) The force generated by a single kinesin molecule against an elastic load. *Proc. Natl. Acad. Sci. U.S.A.* **92,** 574–578
17. Block, S. M., Goldstein, L. S. B., and Schnapp, B. J. (1990) Bead movement by single kinesin molecules studied with optical tweezers. *Nature* **348,** 348–352
18. Shastry, S., and Hancock, W. O. (2010) Neck linker length determines the degree of processivity in kinesin-1 and kinesin-2 motors. *Curr. Biol.* **20,** 939–943
19. Brunnbauer, M., Mueller-Planitz, F., Kösem, S., Ho, T. H., Dombi, R., Gebhardt, J. C. M., Rief, M., and Okten, Z. (2010) Regulation of a heterodimeric kinesin-2 through an unprocessive motor domain that is turned processive by its partner. *Proc. Natl. Acad. Sci. U.S.A.* **107,** 10460–10465
20. Hancock, W. O., and Howard, J. (1998) Processivity of the motor protein kinesin requires two heads. *J. Cell Biol.* **140,** 1395–1405
21. Hancock, W. O., and Howard, J. (1999) Kinesin's processivity results from mechanical and chemical coordination between the ATP hydrolysis cycles of the two motor domains. *Proc. Natl. Acad. Sci. U.S.A.* **96,** 13147–13152
22. Guydosh, N. R., and Block, S. M. (2006) Backsteps induced by nucleotide analogs suggest the front head of kinesin is gated by strain. *Proc. Natl. Acad. Sci. U.S.A.* **103,** 8054–8059
23. Klumpp, L. M., Hoenger, A., and Gilbert, S. P. (2004) Kinesin's second step. *Proc. Natl. Acad. Sci. U.S.A.* **101,** 3444–3449
24. Rosenfeld, S. S., Fordyce, P. M., Jefferson, G. M., King, P. H., and Block, S. M. (2003) Stepping and stretching: how kinesin uses internal strain to walk processively. *J. Biol. Chem.* **278,** 18550–18556
25. Block, S. M. (2007) Kinesin motor mechanics: binding, stepping, tracking, gating, and limping. *Biophys. J.* **92,** 2986–2995
26. Uemura, S., and Ishiwata, S. (2003) Loading direction regulates the affinity of ADP for kinesin. *Nat. Struct. Biol.* **10,** 308–311
27. Shastry, S., and Hancock, W. O. (2011) Interhead tension determines processivity across diverse N-terminal kinesins. *Proc. Natl. Acad. Sci. U.S.A.* **108,** 16253–16258
28. Muthukrishnan, G., Zhang, Y., Shastry, S., and Hancock, W. O. (2009) The processivity of kinesin-2 motors suggests diminished front-head gating. *Curr. Biol.* **19,** 442–447
29. Andreasson, J. O., Shastry, S., Hancock, W. O., and Block, S. M. (2015) The mechanochemical cycle of mammalian kinesin-2 KIF3A/B under load. *Curr. Biol.*, in press
30. Huang, T. G., and Hackney, D. D. (1994) *Drosophila* kinesin minimal motor domain expressed in *Escherichia coli*. *J. Biol. Chem.* **269,** 16493–16501
31. Morrison, J. F. (1969) Kinetics of the reversible inhibition of enzyme-catalysed reactions by tight-binding inhibitors. *Biochim. Biophys. Acta* **185,** 269–286
32. Cheng, Y., and Prusoff, W. H. (1973) Relationship between the inhibition constant (KI) and the concentration of inhibitor which causes 50 per cent inhibition (I50) of an enzymatic reaction. *Biochem. Pharmacol.* **22,** 3099–3108
33. Moffitt, J. R., Chemla, Y. R., and Bustamante, C. (2010) Methods in statistical kinetics. *Methods Enzymol.* **475,** 221–257
34. Uppalapati, M., Huang, Y., Shastry, S., Jackson, T. N., and Hancock, W. O. (2009) in *Methods in Bioengineering: Microfabrication and Microfluidics* (Lee, L. P., and Zahn, J. D., eds) pp. 311–337, Artech House Publishers, Boston, MA
35. Gillespie, D. T. (1977) Exact stochastic simulation of coupled chemical reactions. *J. Phys. Chem.* **81,** 2340–2361
36. Svoboda, K., Mitra, P. P., and Block, S. M. (1994) Fluctuation analysis of motor protein movement and single enzyme kinetics. *Proc. Natl. Acad. Sci. U.S.A.* **91,** 11782–11786
37. Hackney, D. D. (1988) Kinesin ATPase: rate-limiting ADP release. *Proc. Natl. Acad. Sci. U.S.A.* **85,** 6314–6318
38. Ma, Y. Z., and Taylor, E. W. (1995) Mechanism of microtubule kinesin ATPase. *Biochemistry* **34,** 13242–13251
39. Gilbert, S. P., and Johnson, K. A. (1994) Pre-steady-state kinetics of the microtubule-kinesin ATPase. *Biochemistry* **33,** 1951–1960
40. Hackney, D. D. (1994) The rate-limiting step in microtubule-stimulated ATP hydrolysis by dimeric kinesin head domains occurs while bound to the microtubule. *J. Biol. Chem.* **269,** 16508–16511
41. Rice, S., Lin, A. W., Safer, D., Hart, C. L., Naber, N., Carragher, B. O., Cain, S. M., Pechatnikova, E., Wilson-Kubalek, E. M., Whittaker, M., Pate, E., Cooke, R., Taylor, E. W., Milligan, R. A., and Vale, R. D. (1999) A structural change in the kinesin motor protein that drives motility. *Nature* **402,** 778–784
42. Milic, B., Andreasson, J. O. L., Hancock, W. O., and Block, S. M. (2014) Kinesin processivity is gated by phosphate release. *Proc. Natl. Acad. Sci. U.S.A.* **111,** 14136–14140
43. Hackney, D. D. (2005) The tethered motor domain of a kinesin-microtubule complex catalyzes reversible synthesis of bound ATP. *Proc. Natl. Acad. Sci. U.S.A.* **102,** 18338–18343
44. Crevel, I. M., Nyitrai, M., Alonso, M. C., Weiss, S., Geeves, M. A., and Cross, R. A. (2004) What kinesin does at roadblocks: the coordination mechanism for molecular walking. *EMBO J.* **23,** 23–32
45. Rosenfeld, S. S., Xing, J., Jefferson, G. M., and King, P. H. (2005) Docking and rolling, a model of how the mitotic motor Eg5 works. *J. Biol. Chem.* **280,** 35684–35695
46. Cheng, J. Q., Jiang, W., and Hackney, D. D. (1998) Interaction of mant-adenosine nucleotides and magnesium with kinesin. *Biochemistry* **37,** 5288–5295
47. Divita, G., Goody, R. S., Gautheron, D. C., and Di Pietro, A. (1993) Structural mapping of catalytic site with respect to alpha-subunit and noncatalytic site in yeast mitochondrial F1-ATPase using fluorescence resonance energy transfer. *J. Biol. Chem.* **268,** 13178–13186
48. Vertommen, D., Bertrand, L., Sontag, B., Di Pietro, A., Louckx, M. P., Vidal, H., Hue, L., and Rider, M. H. (1996) The ATP-binding site in the 2-kinase domain of liver 6-phosphofructo-2-kinase/fructose-2,6-bisphosphatase. *J. Biol. Chem.* **271,** 17875–17880
49. Woodward, S. K. A., Eccleston, J. F., and Geeves, M. A. (1991) Kinetics of the interaction of 2′(3′)-*O*-(*N*-methylanthraniloyl)-ATP with myosin subfragment 1 and actomyosin subfragment 1: characterization of two acto-S1-ADP complexes. *Biochemistry* **30,** 422–430
50. Uyeda, K., Wang, X. L., Mizuguchi, H., Li, Y., Nguyen, C., and Hasemann, C. A. (1997) The active sites of fructose 6-phosphate,2-kinase:fructose-2,6-bisphosphatase from rat testis: roles of Asp-128, Thr-52, Thr-130, Asn-73, and Tyr-197. *J. Biol. Chem.* **272,** 7867–7872
51. Ma, Y. Z., and Taylor, E. W. (1997) Interacting head mechanism of microtubule-kinesin ATPase. *J. Biol. Chem.* **272,** 724–730
52. Ma, Y. Z., and Taylor, E. W. (1997) Kinetic mechanism of a monomeric kinesin construct. *J. Biol. Chem.* **272,** 717–723
53. Schnapp, B. J., Crise, B., Sheetz, M. P., Reese, T. S., and Khan, S. (1990) Delayed start-up of kinesin-driven microtubule gliding following inhibition by adenosine 5′-[β,γ-imido]triphosphate. *Proc. Natl. Acad. Sci. U.S.A.* **87,** 10053–10057
54. Hariharan, V., and Hancock, W. O. (2009) Insights into the mechanical properties of the kinesin neck linker domain from sequence analysis and molecular dynamics simulations. *Cell. Mol. Bioeng.* **2,** 177–189
55. Yamazaki, H., Nakata, T., Okada, Y., and Hirokawa, N. (1995) KIF3A/B: a heterodimeric kinesin superfamily protein that works as a microtubule plus end-directed motor for membrane organelle transport. *J. Cell Biol.* **130,** 1387–1399
56. Schroeder, H. W., 3rd, Hendricks, A. G., Ikeda, K., Shuman, H., Rodionov, V., Ikebe, M., Goldman, Y. E., and Holzbaur, E. L. F. (2012) Force-dependent detachment of kinesin-2 biases track switching at cytoskeletal filament intersections. *Biophys. J.* **103,** 48–58
57. Okada, Y., and Hirokawa, N. (1999) A processive single-headed motor: kinesin superfamily protein KIF1A. *Science* **283,** 1152–1157
58. Soppina, V., Norris, S. R., Dizaji, A. S., Kortus, M., Veatch, S., Peckham, M.,

and Verhey, K. J. (2014) Dimerization of mammalian kinesin-3 motors results in superprocessive motion. *Proc. Natl. Acad. Sci. U.S.A.* **111,** 5562–5567
59. Okada, Y., and Hirokawa, N. (2000) Mechanism of the single-headed processivity: diffusional anchoring between the K-loop of kinesin and the C terminus of tubulin. *Proc. Natl. Acad. Sci. U.S.A.* **97,** 640–645
60. Romberg, L., Pierce, D. W., and Vale, R. D. (1998) Role of the kinesin neck region in processive microtubule-based motility. *J. Cell Biol.* **140,** 1407–1416
61. Toprak, E., Yildiz, A., Tonks Hoffman, M. T., Rosenfeld, S. S., and Selvin, P. R. (2009) Why kinesin is so processive. *Proc. Natl. Acad. Sci. U.S.A.* **106,** 12717–12722
62. Schnitzer, M. J., Visscher, K., and Block, S. M. (2000) Force production by single kinesin motors. *Nat. Cell Biol.* **2,** 718–723
63. Visscher, K., Schnitzer, M. J., and Block, S. M. (1999) Single kinesin molecules studied with a molecular force clamp. *Nature* **400,** 184–189
64. Albracht, C. D., Rank, K. C., Obrzut, S., Rayment, I., and Gilbert, S. P. (2014) Kinesin-2 KIF3AB exhibits novel ATPase characteristics. *J. Biol. Chem.* **289,** 27836–27848
65. Arpağ, G., Shastry, S., Hancock, W. O., and Tüzel, E. (2014) Transport by populations of fast and slow kinesins uncovers novel family-dependent motor characteristics important for *in vivo* function. *Biophys. J.* **107,** 1896–1904
66. Hoeprich, G. J., Thompson, A. R., McVicker, D. P., Hancock, W. O., and Berger, C. L. (2014) Kinesin's neck-linker determines its ability to navigate obstacles on the microtubule surface. *Biophys. J.* **106,** 1691–1700
67. Brunnbauer, M., Dombi, R., Ho, T. H., Schliwa, M., Rief, M., and Ökten, Z. (2012) Torque generation of kinesin motors is governed by the stability of the neck domain. *Mol. Cell* **46,** 147–158